

AN ABSTRACT OF THE THESIS OF

Na Li for the degree of Master of Science in Mechanical Engineering presented on April 13, 2001. Title: Metallurgy and Superconductivity of Niobium-Titanium-Tantalum Ternary Alloy System.

Redacted for Privacy

Abstract approved: _____

William H. Warnes

The metallurgy and superconductivity of the Nb-Ti-Ta ternary alloy system were studied. The Nb-Ti, and Ta-Ti binary samples, and Nb-Ti-Ta ternary samples were precipitation heat treated under different schedules. After the precipitating heat treatment, the samples were characterized by X-Ray Diffraction (XRD) techniques. Equilibrium binary and ternary phase diagrams based on the different alloy compositions and heat treatment temperatures were developed. The Ta-Ti binary phase diagram is very close to the ASM standard phase diagram. The β -phase boundary of Nb-Ti binary phase diagram developed here is at a higher temperature relative to the ASM standard one. A working ternary equilibrium phase diagram for the Nb-Ti-Ta system has been developed that is based on the experimental measurements and quantitative thermodynamic calculations. Measurements of superconducting critical temperature, T_c , show a good agreement with previous measurements of T_c in the ternary alloys.

© Copyright by Na Li

April 13, 2001

All Rights Reserved

**METALLURGY AND SUPERCONDUCTIVITY OF NIOBIUM-
TITANIUM-TANTALUM TERNARY ALLOY SYSTEMS**

by

Na Li

A Thesis

submitted to

Oregon State University

in partial fulfillment of
the requirements for the
degree of

Master of Science

Presented April 13, 2001
Commencement June 2002

Master of Science thesis of Na Li presented on April 13, 2001

Approved:

Redacted for Privacy

Major Professor, representing Mechanical Engineering

Redacted for Privacy

Head of Department of Mechanical Engineering


Redacted for Privacy

Dean of Graduate School

I understand that my thesis will become part of the permanent collection of Oregon State University libraries. My signature below authorizes release of my thesis to any reader upon request.

Redacted for Privacy

Na Li, Author



ACKNOWLEDGMENTS

I would like to acknowledge the constant support and encouragement received over the years from my professor, William H. Warnes. Anytime I struggled with experimental results, felt disappointed or need assistant, he was always willing to give advices and render aid.

In particular, I wish to thank Alexander Yokochi from Chemistry Department for his guidance with running x-ray analysis and Roger Neilson from College of Oceanography for performing with electron microprobe analysis.

The financial support of the Fermi National Acceleration Laboratory is gratefully acknowledged. Without their support, this project couldn't be fulfilled.

TABLE OF CONTENTS

INTRODUCTION AND BACKGROUND

Introduction and background	1
Literature review	2
Binary phase diagrams	2
Contamination Effect on Binary Phase Diagrams.....	5
Ternary phase diagrams	5
Superconducting properties.....	7
Critical temperature.....	7
Upper critical field	8
Critical current density.....	9
Conclusions	14

EXPERIMENTAL PROCEDURES

16

Sample sources	16
Electron microprobe analysis.....	16
Annealing conditions.....	17
X-ray-diffraction analysis	18
XRD peak fitting routine.....	18
XRD data analysis routine.....	19
Critical temperature measurement	20

RESULTS AND DISCUSSION

22

EMPA results on sample homogeneity	22
Binary systems	23
X-ray diffraction results	23
Phase diagram calculations by regular solution model	28
Contamination effect	33
Kinetics of β and α transformations.....	33
Ternary alloy systems.....	36
Ternary samples and adopted model.....	36
Ternary alloy phase diagrams.....	37

TABLE OF CONTENTS (CONTINUED)

Thermo-calculation phase diagrams.....	37
X-ray diffraction results	37
Diffusion behavior of ternary alloys	40
Critical temperature for binary and ternary alloy systems	42
Conclusions	44
BIBLIOGRAPHY	45
APPENDICES	50
Appendix I. X-ray analysis routine	51
Appendix II. Regular solution model of binary and ternary phase equilibria.....	55
Appendix III. Critical temperature measurement.....	60
Appendix IV. Critical temperature data	62

LIST OF FIGURES

<u>Figure</u>	<u>Page</u>
1. The binary Nb-Ti alloy system at low temperature.....	4
2. The binary Ta-Ti alloy system at low temperature	4
3. The type B ternary diagram from reference	6
4. The schematic of critical temperature measurement	21
5. Ta-Ti x-ray diffraction patterns for different temperature heat treatment.....	24
6. Typical Nb-Ti samples XRD pattern under different heat treatment temperatures	25
7. The binary Ta-Ti alloy system at low temperature	31
8. The binary Nb-Ti alloy system at low temperature.....	31
9. Semilog plot of the diffusivity as a function of the inverse of the temperature for Ta-Ti binary alloy	35
10. Comparison of interdiffusion coefficients of Nb-Ti and Ta-Ti binary systems...	35
11. Type B ternary phase diagram and investigated ternary samples	38
12. Experimental data from precipitating heat treatment at different temperatures in Nb-Ti-Ta ternary alloy system.....	39
13. Extrapolated ternary equilibrium phase diagram for the Nb-Ti-Ta system	40
14. Ternary diffusivity-Lines of constant diffusivity plotted on the Nb-Ti-Ta ternary phase diagram at temperature 400°C	41
15. Ternary diffusivity-Lines of constant diffusivity plotted on the Nb-Ti-Ta ternary phase diagram at temperature 500°C	41
16. Ternary diffusivity-Lines of constant diffusivity plotted on the Nb-Ti-Ta ternary phase diagram at temperature at 600°C	42
17. Critical temperature as a function of alloy compositions.....	44

LIST OF TABLES

<u>Table</u>	<u>Page</u>
1. Lattice parameters of Nb, Ti, and Ta elements	2
2. Critical temperatures of binaries, ternaries, and quaternaries under certain heat treatment conditions	7
3. Upper critical fields of binaries, ternaries, and quaternaries from literature.....	10
4. GLAG theory related parameters determined for binaries and ternaries	11
5. α -Ti precipitates at different heat treatments for ternary similarly processed binary alloys	13
6. J_c vs. magnetic field at different heat treatment at 4.2 K.....	14
7. The sources of samples and heat treatment conditions	17
8. Chemical analysis of ternary samples using electron microprobe analysis	22
9a. Ta-Ti x-ray diffraction data	26
9b. Nb-Ti x-ray diffraction data	27
10. Regular solution parameters for Ti-based stable equilibria.....	29
11a. Ta-Ti binary phase boundary.....	29
11b. Nb-Ti binary phase boundary.....	30
12a. Nb-Ti-Ta ternary β -phase boundary-XRD	38
12b. Nb-Ti-Ta ternary β -phase- boundary-Calculation	39

LIST OF APPENDIX FIGURES

<u>Figure</u>	<u>Page</u>
A1. The atomic scattering factors	54
A2. Free energy representation of formation of ternary phase equilibria	57
A3. Critical temperature measurements	61
A4. Critical temperature verse the heat treatment.....	62

LIST OF APPENDIX TABLES

<u>Table</u>	<u>Page</u>
A1. Multiplicity factors.....	53
A2. The notation used in NbTiTa ternary system	56
A3. Critical temperatures at different aging times and aging temperatures.....	67

LIST OF ABBREVIATIONS, SYMBOLS and NOTATIONS

A	Amper
a	Hexagonal crystal lattice parameter
a₀	Cubic crystal lattice paramater
Ar	Argon
at%	Atomic percent
Avg.	Average
BCC	Body centered cubic (crystal lattice)
c	Hexagonal crystal lattice parameter
°C	Degree Celsius
CSA	Cross section area
CW	Cold work
d	Diameter
D	Interdiffusion coefficient
D₀	Frequency factor
dg	Degree angle
EMPA	Electron microprobe analysis
GLAG	Ginzburg, Landau, Abrikosov, and Gor'kov
H	Magnetic field
H_{C2}	Upper critical Field
HCP	Hexagonal close packed (crystal lattice)
H₀	Upper critical field at absolute zero
h	Hours
Jc	Critical current density
K	Kelvin
Nb	Niobium
NHT	No heat treatment
NT	Niobium-Titanium alloy

pct	Percent of titanium
ppt	Precipitate
R	Gas constant
s	Second
T	Temperature
Ta	Tantalum
Tc	Critical temperature
TEM	Transmission electronic microscope
Ti	Titanium
TT	Tantalum-Titanium alloy
wt%	Weight percent
XRD	X-ray diffraction
V%	Volume fraction
ϵ	Strain
γ	Electronic specific heat coefficient
μ_0	Permeability of free space = $4\pi \times 10^{-7}$
ρ_n	Normal state resistivity

In this thesis, all alloys are in weight percentage except special noticed.

DEDICATION

Dedicated to Mom and Dad.

METALLURGY AND SUPERCONDUCTIVITY OF NIOBIUM-TITANIUM-TANTALUM TERNARY ALLOY SYSTEMS

INTRODUCTION AND BACKGROUND

Introduction:

High Energy Physics has long supported the study of superconductivity, especially the high-field, high current density superconductors. The reason for this has been the attractiveness of superconducting materials for use in accelerator magnets for beam steering, control and focussing. Of the low temperature metallic superconductors one potential candidate for fabricating high field electromagnets is the Nb-Ti-Ta ternary system. The ternary alloys show higher critical magnetic fields than the Nb-Ti binaries as the temperature is decreased. The attractions of these materials for magnet construction are its ductility and ease of handling relative to A-15 intermetallic or ceramic high temperature superconductor (HTS) competitors.

There are many questions about the potential for the ternary alloys, principally relating to fabricability and optimum critical current density at high fields. Recent work, funded at our laboratory by Fermi National Accelerator Laboratory, has used existing literature information to develop an understanding of the equilibrium ternary phase diagram of the Nb-Ti-Ta system, and has provided insight as to the alloy compositions and heat treatments that are likely to lead to higher performance in this system^[1,2]. The previous understanding of the metallurgy of this system has been limited by a lack of information in the literature about the equilibrium properties of the alloys of interest, as well as by a dearth of studies on the precipitation behavior. Both of these limitations can be overcome by additional experimental work on the superconducting alloys with the best potential for high critical field and current density.

Literature Review:

Binary Phase Diagrams

The atomic volume difference among Nb, Ti, and Ta is small. According to JCPDS ^[3] data, the atomic volume difference between Nb and Ta is 0.02 pct and 2.9 pct between Nb/Ta and Ti. A 2% volume difference ^[4] and a 1.3 % diameter difference ^[5] between Nb and Ti are also reported (Table 1).

Table 1 Lattice parameters of Nb, Ti, Ta elements (Å). a_β is the bcc- β phase parameters, and a_α is the hcp α -phase parameter.

	Nb	Ta	Ti	
	a_β	a_β	a_β / a_α	c
value for pure elements [3]	3.3030	3.3058	- /2.9505	4.6826
[6]	3.3067	3.2980	3.3066/2.9512	4.6845
			- /2.9503	4.6831
d (lattice adjacent plane spacing) [6]	1.43	1.43		1.45

The very small atomic size difference between Nb and Ta results in an isomorphous system of continuous series of solid solutions. In NbTi and TaTi binary systems, the BCC elements form a partial miscibility gap with α -Ti (HCP) in the presence of a stable β -phase solid solution (BCC). The major difference between the NbTi and TaTi binary phase diagrams is that the β -phase boundary in TaTi is at lower Ti concentration than that in the NbTi binary system. In other words, the β -phase boundary in TaTi binaries is located at higher temperatures when compared to the same alloy composition in Nb-Ti. All three binary systems have been studied extensively ^[7-18]. The phase diagram of NbTa in ASM ^[18] shows a complete miscibility of Ta and Nb in the solid .

At present, although the author admits that “there is a fundamental difficulty in determining the β transus in this alloy (20 at % to 70 at % Nb) system”, Moffat’s Ph.D. thesis ^[7] has been considered as the most systematic work done on the NbTi binary phase diagram. His results were based mainly on his predictions and the experimental data at high temperatures from others work ^[6-12]. No one, however, has ever done experiments below 600°C because the diffusion rate is believed very slow at low temperature and it takes a long time to reach the equilibrium state.

There are two sets of data representing the Nb-Ti phase diagram, as shown in Figure 1. One is from Kaufman’s prediction ^[11]. This calculation is very close to the experimental data obtained from Hansen ^[8]. Hansen believed that his results represent the conditions close to the equilibrium. Another set of data is from Murray’s prediction ^[10], as well as Brown’s experimental work ^[9]. Although Murray’s work is part of the ASM ^[18] binary phase diagram, Moffat believed that “the resultant negative β phase interaction parameter Murray initialized was acknowledged as being physically unreasonable in this system”. The data in references 19-25 in Figure 1 are experimental measurements of microstructure that are interpreted here with the lever rule to find the β -phase boundary.

All literature data about Ta-Ti binary phase diagrams system is shown in Figure 2. Summer’s ^[15-16] results show a higher tantalum content β -phase boundary than the ASM published data at all temperatures. He didn’t do the experiment below 700°C. However, his extrapolated data at 650°C and 600°C are all higher than that of other’s work. Maykuth’s results ^[17] are closer to the published phase boundary, but still higher than all other works except Summer’s. Chernov, et al ^[26] is very close to the ASM data.

The solubility of Nb and Ta in α -Ti increases as the temperature is lowered. Nb is less soluble in α -Ti than Ta is. In the β -phase, BCC elements lower the transition point of titanium, thus stabilizing the β -phase. So, we call them β -phase stabilizers. Of four elements with partial miscibility with α -Ti alloys (Nb, V, Mo, Ta), Ta has the widest $\alpha+\beta$ two-phase region. Therefore, Ta is the weakest β -phase stabilizer.

Nb-Ti Binary Alloy Phase Diagrams

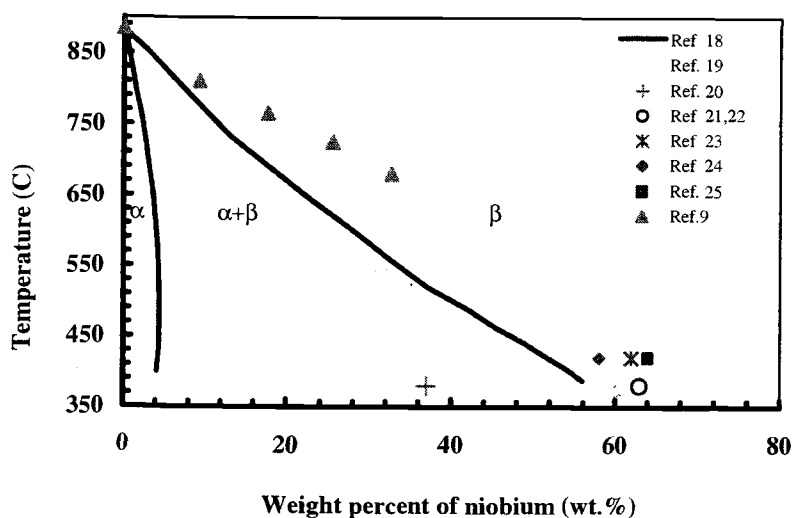


Figure 1. The binary Nb-Ti alloy system at low temperatures. The solid lines indicate the standard binary phase diagram^[18]. The symbols show the experimental results from various references (see legend).

Ta-Ti Binary Phase Diagrams

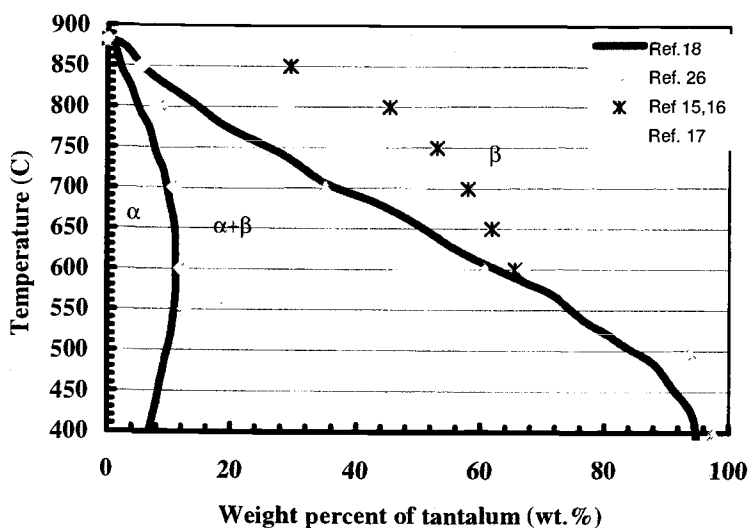


Figure 2. The binary Ta-Ti alloy system at low temperatures. The solid lines indicate the standard binary phase diagram^[18]. The symbols show the experimental results from various references (see legend).

Contamination Effect on Binary Phase Diagrams

When heat-treated at high temperature, the samples are very easily contaminated with oxygen. Contamination may cause the lattice to distort and affect the position of the phase boundary.

These interstitial atoms obtain high thermal energy when they are heated up. It has been shown theoretically that carbon, nitrogen, and oxygen in interstitial solution lower the free energy of the α phase relative to β phase^[7]. The predicted results are shown in Moffat thesis as well^[7]. To demonstrate this effect, Hansen, et al^[8] prepared two different Ti-Mo samples (representing high and low levels of impurities) and found out that the β -phase boundary in high impurity alloys is about 20% higher in temperature than that in low impurity ones.

Ternary Phase Diagrams

There is a very limited amount of work done on the Nb-Ti-Ta ternary composition temperature phase diagrams. In Warnes et al. work^[1], they successfully established ternary diagrams combining temperature and composition information into one plot, as shown in Figure 3. By searching and analyzing the existing literature data on Nb-Ti-Ta ternary alloys and corresponding binary systems, a reasonable prediction of the minimum β -phase boundary position and optimization for the H_{c2} and J_c were proposed^[1]. They believe that most samples studied in the past were either on the lower Ta composition side, or at the top of, the H_{c2} peak. If samples are at a low Ta content, one can never obtain the H_{c2} peak from them because they are far from the H_{c2} peak and the precipitation tie line will never pass through the H_{c2} peak region at all. On the other hand, if samples are at the top of or a little bit off the H_{c2} peak, the precipitating heat treatment will easily overshoot and miss the H_{c2} peak due to the faster kinetics of Ta-ternary alloys.

The other problem suggested by the authors is that the precipitating temperatures have been too low to optimize H_{c2} . As shown in Figure 3, even at 420 °C heat treatment, the predicted β -phase boundary is still on the lower side of the H_{c2} peak.

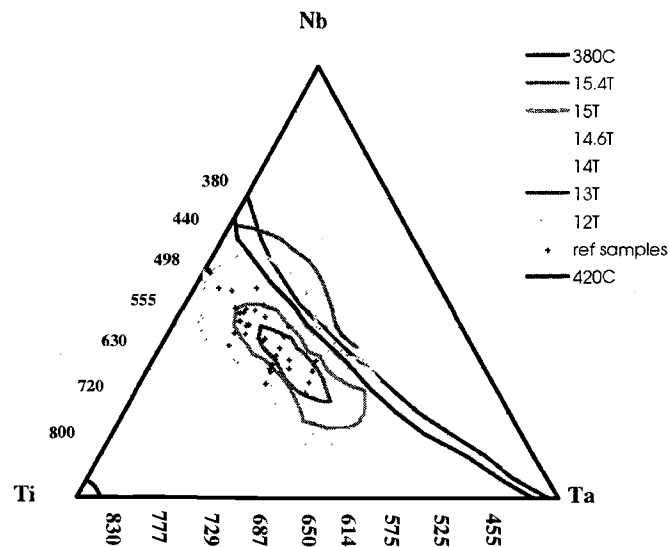


Figure 3. The type B ternary diagram from reference ^[1]. The H_{c2} contour plot at 2.0K, and the 380 °C and 420°C β -phase boundary predicted are also plotted here. The dots are ternary samples investigated up to now.

As far as we know ^[1], 420°C is the highest precipitating heat treatment temperature that has been attempted for optimizing high H_{c2} or J_c in Nb-Ti-Ta ternary system. The suggested solution for this is to use higher precipitating temperature to heat-treat the samples of the right composition. This is also the guideline for us to deal with our samples later on. We haven't seen any other reports in the literatures on Nb-Ti-Ta ternary phase diagrams.

Superconducting Properties

Critical Temperature (T_c)

Generally, the critical temperature is considered to decrease by additions of Ta, Hf, and Zr to the binary system with Nb due to the lower critical temperature of these elements compared to Nb. The critical temperatures for pure Nb, Ta, Hf, Zr are 9.5 K, 4.4 K, 0.12

K, and 0.55K respectively. However, for up to 6 at % Ta the decrease in T_c is very small^[27]. T_c of the alloys is affected by heat treatment. Both aging time and aging temperature influence T_c .

In the study of the ternaries, Wada et al found that in the NbTiHf ternary alloy, 3 at % Hf increases T_c at all aging temperatures^[28]. The addition of Hf (Ti 40 at % Nb 3 at % Hf) causes a T_c increase of about 0.3 K over Ti-40 at % Nb. More than 6 at % Hf additions, decrease T_c when the aging temperature is below 600°C. With an aging temperature of 800°C, addition of Hf tends to increase the critical temperature. X-ray analysis revealed that aging at 800°C caused significant precipitation of α -phase in high Hf alloys.

Table 2. Critical temperature (K) of binaries, ternaries and quaternaries under certain heat treatment conditions.

Alloys (wt. %)	T_c	references
TERNARIES		
NbTiTa20	9.1(extrusion + 80% cold drawing)	29
NbTiTa12	9.1 (extrusion + 80% cold drawing)	29
NbTiTa20	8.7 (homogenized at 1300°C/8h)	29
NbTiTa12	8.99 (homogenized at 1300°C/8h)	29
Nb25Ta 45Ti	8.2	30
Nb15Ta 44Ti	8.85	30
Nb40Ti18Ta	9.45 (450°C/60h)	19
Nb41Ti28Ta	9.4 (375°C/40h)	19
Ti38Nb16Ta	8.33	27
Ti16Nb44.8Ta	7.17	27
Nb62.5Ti7.21Hf	9.5	28
Nb64.5Ti1Zr	6.5, 8.4 (380°C/800h)	20
BINARIES		
Nb65Ti	7.3 (380°C/80h)	20
Ti50Nb	8.52	27
Nb46.5Ti	8.9,9.42 (372°C/40h)	30, 19
Nb18.1Ti	10.1	30

The critical temperature increases with the aging time of NbTiZr^[20]. The critical temperature of Zr specimens aged at 380°C for 800 hours increases from 6.5 K (see Table 2) up to values of about 8.4K. Panek attributes the enhancement of T_c with increasing aging time to the Nb enrichment of the matrix that accompanies the α -Ti precipitation, as determined using TEM. The critical temperature of Hf ternary specimens aged above 600 °C can be increased from 8.0K~8.3 K up to 9K^[20]. Aging time or temperature can have a significant effect on critical temperature. The T_c of a variety of NbTi ternary and binary alloys under a range of process conditions is given in Table 2.

Upper Critical Field (H_{c2})

The upper critical field of binary NbTi is normally suppressed by spin-orbit-coupling. Alloying with an element of high atomic number, such as Ta, Hf, or Zr can suppress the paramagnetic limitation, and reduce spin-orbit-coupling through spin-orbit-scattering. There should be a stronger enhancement of H_{c2} at lower temperature because at lower temperature, the paramagnetic limitation becomes stronger.

H_{c2} is temperature dependent as, $H_{c2} \sim [1-(T/T_c)^2]$. At 4.2K, the enhancement of H_{c2} in the ternaries is slight, with small increases of 0.15 tesla^[20], 0.2 tesla^[19], and 0.3 tesla^[31] reported. This is shown in Table 3. At 4.2K, no significant difference is seen between the H_{c2} of the binaries and Ta-ternaries. The highest H_{c2} (13.6 Tesla) at 4.2K is observed in Nb₂₂Ti₂₂Zr.

In the NbTiTa case, replacing Nb with Ta enhances H_{c2} (4.2 K) up to 10 to 15Ta depending on Ti concentration^[32]. At around 2.0 K, H_{c2} can be raised from 14.1 tesla for the best binary (Nb 46.5Ti) to 15.5 tesla (Nb 42Ti 19Ta)^[31], and 15.4 tesla (Nb₄₃Ti₂₅Ta, Nb₄₁Ti₂₈Ta)^[20, 31, 33] for the ternary alloys.

H_{c2} is also a function of normal state resistivity (ρ_n), electronic specific heat coefficient (γ), and critical temperature (T_c). At 0 K, the relation is given by GLAG theory^[31] as:

$$\mu_0 H_0 = 3.1 \times 10^3 \gamma \rho_n T_c \text{ (tesla)}$$

Equation 1

It is reported ^[31] that when replacing Nb by Ta, T_c decreases slowly, and γ , ρ_n do not change. This therefore results in a gradual decrease in H_0 . By replacing Ti by Hf, a rapid reduction of T_c and γ results in a decrease of H_0 . Suenaga reported ^[30] that for Nb-rich alloys in the 64 at % Ti series, a decreased T_c and ρ_n due to the replacement of Ta for Nb caused a decrease in critical field. From Table 4, it can be seen that adding a third element produces higher normal state resistivity and lower critical temperature (except for 2.5 Hf-ternary in which Hf-concentration is too low to influence the overall critical temperature) compared to the binaries. The concentration of Ta does not strongly influence the ρ_n , while in Hf-ternaries, ρ_n increased obviously with the Hf concentration. According to Hawksworth ^[31], the H_0 of the ternaries is equal to or less than the binaries, except for the case of 5 at % Ta that increased the H_{c2} (see Table 4).

Critical Current Density (J_c)

Adding the third component increases the diffusion rates of Ti, and therefore accelerates the precipitation kinetics of α -Ti ^[20]. So, generally, NbTiTa ternary alloys produce 10% more volume fraction of precipitates for the same heat treatment schedules than the binaries. However, the precipitate size in the ternary is larger than that in the binary. Taillard ^[21] found growth of alpha precipitates on subband cell walls after heat treatment. In the ternary alloys, however, a relatively low concentration of a third element can suppress during cooling and accelerates precipitation of the stable α -phase. Also, a large pre-strain (6.4~7) can suppress the ω -phase in both binary and ternary alloys. The ω -phase is a metastable phase which grows isothermally. Larbalestier ^[37] stated that Zr additions form precipitates more easily due to the larger atomic size of Zr. Precipitation of α -Ti containing Zr may therefore form more rapidly than in binary alloys. However, replacing Ti by Zr may result in a reduction in the quality of α -Ti precipitate for flux pinning ^[23],

Table 3. Upper critical fields (Tesla) of binaries, ternaries and quaternaries from literature.

Alloy (wt %)	4.2K	2.0 K	References
TERNARIES			
Nb44.8Ti-12.3Ta	10.4 ($\epsilon=4$)	13.3~13.4 (2.2K); 14.1, 14.3 (1.85K)	29, 34
Nb42.6Ti20.4Ta	10.3 ($\epsilon=4$)	13.4~13.8 (2.2K); 14.3, 14.5 (1.85K)	29, 34
Nb44Ti25Ta	10.4	14.4	35
Nb45Ti25Ta	10.9	14.8	32
Nb44Ti15Ta	11.6	15	32
Nb45.7Ti13.3Ta	11.6	15	31
Nb43Ti25Ta	11.6	15.4	31
Nb40.5Ti35.31Ta	11.1	15.3	31
Nb33.4Ti44.5Ta	10.9	15.2	31
Nb42Ti19Ta		15.5	19
Nb41Ti13Hf		14.5	19
Nb44.7Ti6.7Hf	11.3	14.35	31
Nb40.9Ti12.7Hf	11	14.5	31
Nb34Ti23Hf	10.4	14.2	31
Nb22Ti22Zr	13.6		31
NbTi15Ta *		14.3 (1.8K)	22
NbTi25Ta *		14.7 (1.9K)	22
Nb40Ti18Ta	11.03, 11.7	13.53, 15.2	20, 33
Nb41Ti28Ta	10.25, 11.3	14, 15.4	20, 33
Nb43.9Ti14Ta		14.3	34
QUARTERNARIES			
Nb39Ti24Ta6Zr	13.1		31
Nb38Ti26Ta6Hf	11.3	15.3	31
BINARIES			
Nb46.5Ti	10.53, 11.3, (--),	13.28, 14.1, 14.2	20, 33, 36
Nb9.82at.%Ti	10.3, 11.3 (--)	13.7, 14.1, 14.2	35, 32, 19
Nb49Ti	12.2		31
Nb38Ti	11.4		31
Nb50Ti		12.7 (1.8K)	22
Nb48Ti	11.5	14.25	31

Table 4. GLAG theory related parameters determined for binaries and ternaries ^[31].

Alloys (at%)	ρ_n (G Ω .m)	γ ($\frac{\mu J}{mm^3 K^2}$)	T _c (K)	H ₀
Nb64.2Ti	6.5	0.92	9	16.5
Nb65Ti5Ta	6.8	0.9	8.9	16.7
Nb65Ti10Ta	6.7	0.93	8.6	16.5
Nb65Ti15Ta	6.9	0.94	8.15	16.2
Nb65Ti20Ta	6.7	0.92	8.1	16.5
Nb62.5Ti2.5Hf	6.8	0.87	9	16.4
Nb60Ti5Hf	6.9	0.91	8.5	16.4
Nb55Ti10Hf	7.25	0.83	8.35	15.45

and thus the magnitude of J_c. Accelerated α -Ti precipitation is also found in the Ta-ternaries. This is believed to be due to the fact that the Ta is a weaker β -phase stabilizer than Nb ^[29].

In the binary system, J_c increases proportionally to the α -phase volume fraction. Lee ^[5] expressed the J_c as a V% of α -Ti precipitate as: J_c=120 V%+675 (5 tesla) and J_c = 41 V% +470 (8 tesla). However, in NbTiTa, NbTiHf, and NbTiZr ternary systems, although a higher α -precipitate volume fraction than binary is observed, J_c is in general lower than that in binary, as shown in Table 5. Although the ternary has a higher volume fraction of alpha precipitates, it also has a larger precipitate size. J_c relates both to the alpha precipitate size and the volume fraction.

J_c is dependent on the final strain after last heat treatment. Addition of Zr produces a significant ($\Delta\epsilon \geq 1$) shift of strain at peak J_c to lower strain ^[23]. Also, the J_c peak is brought down to lower value. However, some studies have shown that the J_c of the ternary alloys is somewhat independent of final strain ^[23,38-39]. One might expect that the lower strain to peak J_c in the ternaries to coincide with a relatively smaller precipitate. However, this is

not always the case. From Table 5, it is hard to get a conclusion that J_c increases with either precipitate size or mean cross section area.

An aggressive heat treatment was suggested^[24] to improve the precipitate volume fraction in the ternaries. J_c increases with the heat treatment temperature until it reaches the peak at 475°C. Extending the treatment temperature or time can increase the precipitation, as shown in Table 5. However, Shimada shows in his work that there was no benefit or even worse from prolonged heat treatment time for high field (7 tesla) J_c . Another way to increase the precipitation rate is to replace Nb with Zr rather than with Ti^[23-24]. The later approach may deteriorate H_{c2} and thus high field properties.

High field J_c near H_{c2} is well known to be less sensitive to heat treatment and microstructure than at lower field^[31]. As shown in Table 6, heat treatment is effective in improving low field J_c .

At high magnetic fields, the dependence of J_c on H is large and then the upper critical field becomes the dominant factor in determining J_c . Of ternary alloys, Nb 65 at % Ti 10~12.5 at % Ta is about the best for high field use because its upper critical field is the maximum (Table 3).

There is a report^[38-39] that at low magnetic field (5 Tesla and 7Tesla), lower Ta ternary alloy (Nb44Ti8Ta) has higher critical current density than higher Ta ternary alloy (Nb43Ti25Ta). However, at high magnetic fields (12 Tesla), higher Ta ternary alloys, such as 25Ta, showed a better performance than the 8Ta.

Table 5. α -precipitate at different heat treatments for ternary and similarly processed binary alloys.

Alloy (wt.%)	V% of α -Ti Heat Treatment ^b		Avg. α -Ti d (nm)	Mean CSA (nm ²)	Jc (A/mm ²) (5Ts, 4.2K)	Jc (A/mm ²) (8Ts, 4.2K)	references
45Ti15Ta/Nb47Ti ^a	18/17	2X80h/380°C			2325/	927/1174	35
45Ti15Ta/Nb47Ti	20.1/16.5	2X80h/ 420°C					35
45Ti15Ta/Nb47Ti	24-25/22	3X40h/380°C					35
45Ti15Ta/Nb47Ti	28/24	4X40h/380°C					35
45Ti25Ta/Nb46.5Ti	25.2/17.8	1.5h /800° C	123/107		2000/2800	290/950	40
45Ti25Ta/Nb46.5Ti	23.3/	40h /375°C	112		2000/3000	290/950	40
45Ti25Ta/Nb46.5Ti	24.8/18.6	CW	127/114		2000/3000	240/950	40
44Ti15Ta/Nb46.5Ti	25/21	3x80/420° C	203/140	32300/15500			41
44Ti15Ta /Nb46.5Ti	27/24	5x80/420° C	163/194	20870/29660			41
46.1Ti1.9Zr/Nb46.5Ti	14/21	3x80/420° C	46/181	5095/41882	3035/3200	1350/750	23
48.9Ti3.8Zr/Nb53Ti	16/28	3x80/420°C	65/82	4846/12327	2800/3200	1100/750	23
40Ti18Ta/Nb46.5T	13.7-14.5	4X40/375° C	114-118		2265-2497	1221	20
41Ti28Ta/Nb46.5Ti	16.4/		107		1840	812	20
Nb45Ti15Ta	25/22	3X40h/380° C		24x2.7	2370/2580	910/1220	21
Nb45Ti15Ta	28/24	4X40h/380° C		24x2.7	2810/3050	900/1220	21
Nb45Ti15Ta	18/17	2X80h/380° C		33x3.8	2280/2570	910/1200	21
Nb44.4Ti15Ta	12.5	6h/405°C+ 20h/420°C+ 80h/420°C			1700	825	42,43,44
Nb44.4Ti15Ta	14	3h/300°C+ 6h/405° C+ 80h/420° C			2250	900	42,43,44
Nb44.4Ti15Ta	16.25	2x3h/300° C+ 6h/405°C			2300	950	42,43,44
Nb44.4Ti15Ta	21	2x3h/300°C+ 80h/420°C			2700	1050	42,43,44
Nb44.4Ti15Ta	21				2800		42,43,44
Nb41Ti28Ta		3x40h/450° C			2647	843	25
Nb44Ti17Ta		3x40h/450°C			2671	992	25
Nb46Ti12Ta		3x80h/450° C			3075	959	25
Nb44Ti17Ta(multi-)		3x80h/375°C			2534	848	25
Nb44Ti17Ta(multi-)		4x80h/375° C			2724	785	25
Nb44Ti17Ta(multi-)		20h/450° C+2x80h/375° C			2637	786	25
Nb41Ti28Ta		5Ts, 3x84h/425° C, 8Ts, 1x48h/425° C			2550	821	24
Nb43Ti20Ta		4x48h/380°C			2170	800	43, 34
Nb43Ti20Ta		2x6h/350°C+1x40h/380°C			1970	780	43, 34
Nb43Ti20Ta		5x12h/350°C			1200	750-800	34
Nb43Ti20Ta		5x12h/380°C			1800	750-800	34
Nb45Ti12Ta		4x48h/380°C			2250	825	34
Nb45Ti12Ta		2x6h/350°C+1x40h/380°C			2000	900	34
Nb45Ti12Ta		5x12h/350°C			1650	850	34
Nb45Ti12Ta		5x12h/380°C			1850	850	34
Nb44Ti14Ta		5x12h/400°C			2500	1150	34
Nb44Ti14Ta		5x12h/350°C			1990	1000	34
Nb47Ti		5x12h/350°C			1280	700	34
Nb44Ti14Ta							34

^a ternary/binary

^b number of heat treatment x hours/ temperature (°C)

Table 6. J_c (A/mm²) vs. magnetic field at different heat treatment at 4.2K^[29].

Field (Tesla)	45 h	85 h	200 h
5	1850	2245	2200
6	1490	1650	1550
7	1125	1125	1000
8	650	625	490

Conclusions:

From studies done and reported in the literature, the following conclusions are drawn:

1. Uncertainty is still exists not only in Ta-Ti, but also in the Nb-Ti binary phase diagram.
2. The Nb-Ti-Ta ternary temperature-composition phase diagram is unknown. Warnes^[1] gives us a pretty good outline to start with.
3. At 4.2 K, even the best ternary alloys showed no significant improvement in either critical field or critical current density. At low temperature, the Ta-ternary can perform much better than the binary does.
4. NbTiZr or NbTiHf conductor did not perform as well as NbTiTa in high field^[23].^[35] When used in high field, NbTiTa has been shown to have significantly higher current density and critical field than NbTiZr or NbTiHf.
5. Cold work after the heat treatment is found to be more effective in increasing J_c in high fields than in low field for NbTiHf. Cold work plays a critical role in high field J_c performance (8 Tesla).
6. Critical current density depends strongly on the heat treatment. However, the size of α -precipitate does not produce a consistent effect on J_c . In general, it is believed that a smaller α -precipitate size is a good pinning center and therefore results in a higher J_c .

7. Homogeneous NbTiTa yields higher J_c than inhomogeneous composite because homogeneous starting material produces smaller more uniform precipitation, and thus raises J_c .
8. Large prestrains of 6.4~7 are required to suppress the deleterious ω -phase in the Ta-ternaries.
9. Binary alloys have a lower volume fraction of alpha precipitate, but higher J_c than similarly processed ternaries.

EXPERIMENTAL PROCEDURES

In order to better understand the equilibrium ternary phase diagram, several experiments were undertaken: EMPA, XRD, and T_c measurement. The as-received samples were basically divided into two sets. One set of these as-received samples was examined under electron microprobe analysis to determine the impurities of the sample. Another set of as-received samples was heat-treated under different schedules (as shown in Table 7), and then XRD was done to identify the phase composition of these samples. Finally, after the XRD test, the critical temperature of the second set of samples was measured. The details are described below.

Source of Samples:

Binary samples were obtained from Oremet-Wah Chang, Albany, Oregon. Ternary samples were obtained from Intermagnetics General Corporation, Waterbury, Connecticut. Bulk samples were cleaned using acetone and methanol. Multifilamentary samples were put into acid to remove the copper, and then cleaned.

Electron Microprobe Analysis (Impurity-Analysis):

Electron microprobe analysis was carried out on four out of six ternary samples in the as-received state to determine their composition and the homogeneity. Nb₂₄Ta₄₉Ti, Nb₁₈Ta₃₉Ti, Nb₁₇Ta₄₄Ti, and Nb₁₅Ta₅₁Ti were encapsulated in conductive mounting compound (PSI-212-1). EMPA was done in The College of Oceanic and Atmospheric Sciences at Oregon State University. Two scans were made of each of the samples examined. The line measurement consisted of ten point analyses evenly spaced along a 10 μm line. The random measurement chose 10 points randomly from the filament cross-section.

Annealing Conditions:

The second set of as-received samples was prepared basically in two groups. One group was prepared in our Lab while the other set was prepared in the Chemistry Department at Oregon State University.

All samples were cleaned and wrapped in the zirconium foil and then placed into a quartz tube. One end of the quartz tube was sealed and the other end of the tube was connected to a mechanical vacuum pump. Samples prepared in our lab were placed at the sealed end and continuously evacuated for about 36 hours before placing in the tube furnace for the heat treatment. The quartz tube with samples in it was then put into the oven at the specified temperature for 300 hours. After turning off the oven, the pump was kept pumping until the samples cooled down (generally this took about another 24 hours), and then the samples were taken out.

Investigated binary and ternary samples and heat treatment schedules are listed in Table 7 below:

Table 7. The sources of samples and their heat treatment conditions

BINARIES						
Samples	NbTi			Ta50Ti		
Composition (wt. %)	46.5Ti (bulk)	46.5 Ti (wire)	55Ti (bulk)	(bulk)		
Annealing Conditions	400°C/300h	400°C/300h	400°C/300h	400°C/300h		
	450°C/300h	450°C/300h	450°C/300h	450°C/300h		
	500°C/300h	500°C/300h	500°C/300h	500°C/300h		
	550°C/300h	550 °C/600h	550 °C/600h	550 °C/300h		
			600 °C/600h	600 °C/600h		
NB-TI-TA TERNARIES						
Composition (wt. %)	12Ta46Ti (multi-)	15Ta51Ti (mono-)	17Ta44Ti (mono-)	18Ta39Ti (bulk)	24Ta49Ti (mono-)	28Ta41Ti (mono-)
Annealing Conditions	400°C/1000h	400°C/1000h	400°C/1000h	400°C/1000h	400°C/1000h	400°C/1000h
	450 °C/300h	450 °C/300h	450 °C/300h	450 °C/300h	450 °C/300h	450 °C/300h
	500 °C/300h	500 °C/300h	500 °C/300h	500 °C/300h	500 °C/300h	500 °C/300h
	550 °C/600h	550 °C/600h	550 °C/600h	550 °C/600h	550 °C/600h	550 °C/600h
	600 °C/600h	600 °C/600h	600 °C/600h	600 °C/600h	600 °C/600h	600 °C/600h

The samples in italic are evacuated by argon.

- multi-: means the samples were in multi-filimentary form
- mono-: means the samples were in mono-filimentary-form

After heat treatment, samples with active pumping were slightly surface-oxidized, depending on the annealing temperature. In order to remove the oxidized layer, samples were surface-polished and cleaned again.

Those samples prepared in Chemistry Department were evacuated as we did in our lab. The samples were then being back filled with argon gas in order to get rid of the oxygen contamination. After being back-filled with argon gas, the quartz tube was sealed at the open end too.

After heat treatment, all bulk samples were filed into powder using a fine file. The wire samples were cut into tiny pieces. All samples were mounted within sample holders for the XRD measurement. Two types of sample holder were used. One was 25-mm in diameter with Vaseline as an adhesive material, the other one was 6 mm in diameter with double-sided tape as the adhesive material. Experimental results showed that there was no significant difference between XRD results from these two types of sample holders.

All ternary samples, binary Ta50Ti and Nb55Ti at 600°C and Nb46.5 Ti at 550°C were back-evacuated under argon condition except at 400°C.

X-Ray-Diffraction Analysis:

X-Ray Peak Fitting Routine

Diffraction Patterns were recorded using a Siemens D5000 diffractometer. In all cases the intensity measurements were made at room temperature with a Cu K α ($\alpha_1=1.5406\lambda$, $\alpha_2=1.5443\lambda$) x-ray source. The data was collected over the 2θ ranging from 35 degrees to 100 degrees because the highest intensity peaks of both α -Ti HCP and β -Nb/Ta BCC phases lie in this range. The x-ray was scanned at a step size of 0.01 and 0.02 degree using a step-counting time between 1 second to 3 seconds. The peaks in diffraction intensity at 0 K are governed by Bragg's Law: $n\lambda = 2d\sin\theta$, where n is an integer, λ is

the x-ray wavelength, d is the spacing between atomic planes, and 2θ is the scattering angle in the plane of the source and detector. At the most basic level, XRD may be used to determine the lattice parameter (λ , θ are known), crystal structure (we weren't concerned with it here), and phase composition (as described in Appendix i).

The observed x-ray diffraction patterns were modeled by a Gaussian function or a Lorentzian function, and fit using a least squares fitting program in order to determine the peak shapes and correct for peak overlap. The refinement was performed assuming n diffraction peaks (we set up the maximum number of fitting peaks to five, but it's easy to change the program), and the fitting parameters of each peak were a) offset of the background; b) peak position; c) full-width-half-maximum (FWHM); and d) intensity. In our experience, the Lorentzian function fits the data better in most cases. This may be attributed to the interesting characteristics of Lorentzian distributions. The Lorentzian function does not diminish to zero as rapidly as in Gaussian's distribution, so it can pick up data along the "tail" and therefore gives the better fitting result. This program is almost user independent.

X-ray data analysis routine

Using the peak-separated and fit XRD data, an intensity ratio of the α to β phase was obtained, as well as the Lorentzian factors, structure factors and multiplicity factors (see Appendix I for details). Once C_α/C_β is found, the value of C_α can be obtained from following relationship:

$$\frac{I_\alpha}{I_\beta} = \frac{R_\alpha C_\alpha}{R_\beta C_\beta} \Rightarrow \frac{C_\alpha}{C_\beta} = \frac{I_\alpha R_\beta}{I_\beta R_\alpha} \quad \text{Equation 2}$$

The additional relationship $C_\alpha + C_\beta = 1$ is used together with above equation to get the composition of both phases.

After the compositions were obtained, the lever rule was applied to calculate the mass fraction of certain phases.

$$M_{\alpha}^i = \frac{C_{\beta}^i - C_A^i}{C_{\beta}^i - C_{\alpha}^i} \quad \text{Equation 3}$$

Where: M_{β}^i is mass fraction of β phase calculated from concentration of element i , C_{β}^i is the concentration of element i in β phase, C_{α}^i is the concentration of element i in α phase and C_A^i is the overall concentration of element i in the alloy.

Critical temperature measurement:

The critical temperatures were measured using a Tc probe built by Dr. Warnes and previous graduates in the Cryogenic Lab.

In this probe, there are three coils: excitation coil, pick-up coil, and a set of witness coils. The schematic of critical temperature measurement is shown in Figure 4. The excitation coil at the bottom of the probe is used to produce a magnetic field around the sample. Pick-up coil on the top of the probe is aligned with excitation coil and used to pick up the signal. The sample will be sandwiched in between. The witness coils were composed of Nb coil and Pb coil connecting in series and used as calibration coil due to the fact that Tc of pure Nb and Pb are known to be 9.3 K and 6.9 K respectively:

The Cernox thermometer is embedded into the probe in order to control the temperature around the sample. The heater is wound all way around the aluminum plate sample holder, and thermometer is embedded into the aluminum plate. The details are described in report ^[2]. The measurement uses the Messiner effect mechanism which says that after superconducting material is cooled down below its Tc, the magnetic lines can't pass through the superconductor any more. Or in other words, the superconducting materials will shield the magnetic field out when it is in the superconducting state.

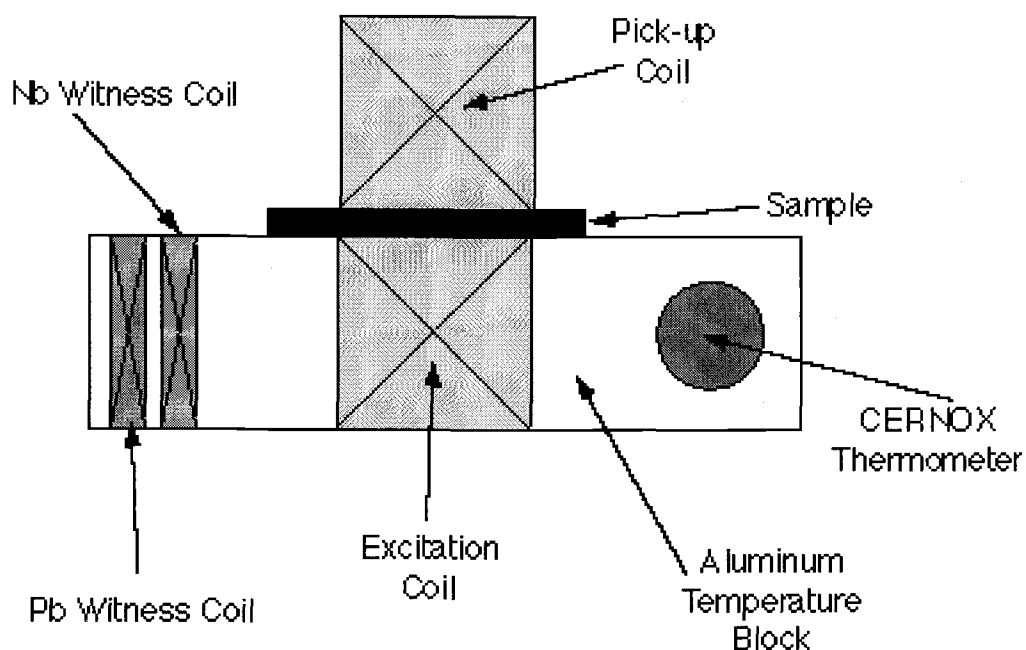


Figure 4. The schematic of critical temperature measurement. The probe is composed of an excitation coil at the bottom of the probe and used to produce a magnetic field. The pick-up coil on the top of the probe is aligned with excitation coil and used to pick up the signal. The two other coils: Nb and Pb coils connected in series and are used to calibrate the data later on. The Cernox thermometer is embedded into the probe in order to control the temperature around the sample.

RESULTS AND DISCUSSION

The Nb-Ti, Ta-Ti binary and Nb-Ti-Ta ternary equilibrium phase diagrams all exhibit a two-phase equilibrium between α -HCP, and β -BCC phases. The temperature of the $\alpha \rightleftharpoons \beta$ transformation of titanium gradually decreases with increase in the concentration of niobium and tantalum. At the titanium apex of the ternary triangle diagram there is a small region of α solid solution based on the titanium and bordering on the two-phase region ($\alpha + \beta$).

EMPA Results on Sample Homogeneity:

From the EMPA data (see Table eight), we can see that titanium has the biggest variation. The most concern is on the Ta due to its high melting temperature and might least be melted. In contrast, the Ti is the most likely to disappear during the melting. All three elements show a variation of less than 1 wt%. This indicates a reasonable homogenous starting sample. EMPA data for two of the samples (Nb₄₆Ti₁₂Ta and Nb₄₁Ti₂₈Ta) are lacking.

**Table 8. Chemical analysis of ternary samples using electron microprobe analysis.
All compositions are given in weight percent.**

	Nb avg.	Nb Stddev	Ta avg.	Ta Stddev	Ti avg.	Ti Stddev
Nb ₅₁ Ti ₁₅ Ta line	33.85	± 0.27	14.97	± 0.35	51.47	± 0.55
Nb ₅₁ Ti ₁₅ Ta random	34.00	± 0.14	15.00	± 0.32	50.81	± 0.71
Nb ₄₄ Ti ₁₇ Ta line	39.62	± 0.38	17.94	± 0.33	42.52	± 0.62
Nb ₄₄ Ti ₁₇ Ta random	39.48	± 0.42	17.40	± 0.75	42.52	± 1.06
Nb ₃₉ Ti ₁₈ Ta line	42.97	± 0.20	19.61	± 0.70	37.39	± 0.80
Nb ₃₉ Ti ₁₈ Ta random	43.09	± 0.19	18.49	± 0.74	38.41	± 0.82
Nb ₄₉ Ti ₂₄ Ta line	27.39	± 0.25	22.75	± 0.67	49.64	± 0.94
Nb ₄₉ Ti ₂₄ Ta random	27.31	± 0.35	23.12	± 0.75	48.94	± 0.76

Binary Alloy Systems

X-Ray Diffraction Results

The x-ray diffraction data of Ta-Ti and Nb-Ti at different temperatures are shown in Figures 5 and 6 respectively. In Ta-Ti, at low heat treatment temperatures there is not a distinct separate $40^\circ\alpha$ -peak. The α -phase peak starts to become obvious at 500°C , and becomes even more distinguishable from the β -phase peak at 550°C . This indicates the diffusion rate becomes faster at 500°C , and faster yet at 550°C . In the Nb-Ti binary system, the XRD pattern is less obvious than that in Ta-Ti system, even at 500°C (Figure 6). This suggests that Nb-Ti has a more sluggish diffusion rate than that in Ta-Ti. The diffusivities will be discussed later. NbTi bulk samples didn't show obvious traces of the two phases. However, the 40° α -phase peak appears in heat-treated wire samples at 500°C and 550°C , as shown in Figure 6. At 550°C , the 63° α -Ti peak appears too. Using longer scanning time and smaller step size, the 40° -degree peak can be seen, but it is quite small at 550°C . This indicates wire samples have much faster kinetic than the bulk samples. However, the composition point we tested is so close to the β -phase boundary at 550°C , and the volume fraction of α -Ti is very small, and therefore results a very small intensity peak.

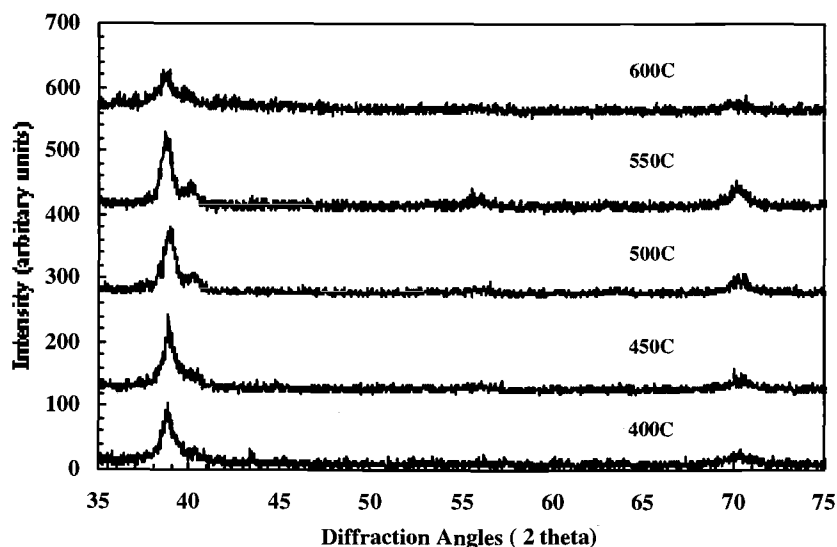


Figure 5-a. Tantalum-titanium x-ray diffraction pattern for different temperature heat treatments. The 40 degree alpha peak becomes obvious starting from 500°C, as well as 55 and 70 degree peaks. The intensity of 600 °C shrinks, as well as the alpha phase peak at 40 degrees. The small angle and long time run for 600 °C shows that alpha phase peak at 40 degree is still visible. All sample data here are taken at 0.02dg/s.

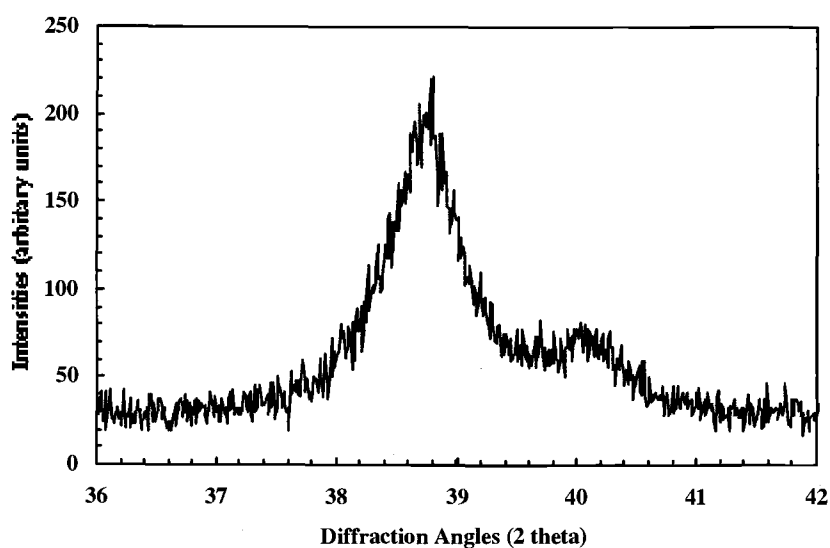


Figure 5-b. Tantalum-titanium XRD pattern for a 600°C heat treatment. This was obtained by step-size of 0.01 dg/2s.

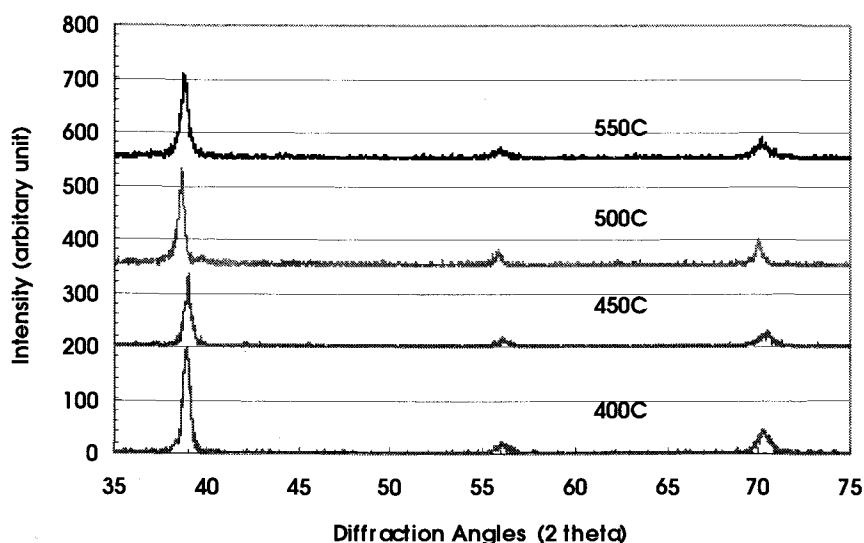


Figure 6. Typical Niobium-titanium samples XRD pattern under different heat treatment temperatures.

Even though distinct separate α - and β - phase peaks do not always appear in the XRD data, the asymmetric peak near 40° can be analyzed as two separate overlapping diffraction peaks. To find the individual peak intensities, the XRD data were analyzed by a custom peak fitting routine. The results are shown in Table 9. The intensity ratio of β phase to α phase of TT start to rise from 500°C , but shrank at 600°C . This indicates that diffusion rate rise up at 500°C . At 600°C , although the kinetics is faster, the V% of α -Ti ppt is smaller, and therefore the intensity peak ratio is smaller too.

Unfortunately, we were not able to get the experimental data at temperatures higher than 650°C for Ta-Ti due to the sample composition limitation. From TaTi binary β -phase diagrams, it is seen that at a composition of Ta50 wt%Ti, the 650°C is in a single β -phase region. We don't have experimental data to present at temperatures below 450°C . Actually, it is almost impossible to get this system to equilibrium at such temperatures within our lifetime. However, thermodynamic calculations allow us to extend our work to where the experiment couldn't reach, as discussed in the next section.

Table 9-a. Ta-Ti X-Ray Diffraction Data

Beta-Phase					
<u>2θ</u>	<u>hkl</u>	<u>lorentz-polarization factor</u>	<u>multiplicity factor</u>	<u>structure factor</u>	<u>Intensities</u>
38.88	110	6.8016	12	58.1933	72.39
55.97	200	2.6107	6	50.9756	21.41
70.2	211	1.4301	24	46.0275	28.15
38.90	110	6.7930	12	58.1843	220.1
55.99	200	2.6081	6	50.9679	25.37
70.20	211	1.4242	24	45.9897	44.24
38.74	110	6.8625	12	58.2566	234.6
55.94	200	2.6146	6	50.9872	37.07
70.32	211	1.4182	24	45.9513	65.87
Alpha-Phase					
<u>2θ</u>	<u>hkl</u>	<u>lorentz-polarization factor</u>	<u>multiplicity factor</u>	<u>structure factor</u>	<u>Intensities</u>
39.94	101	6.3623	12	14.0120	14.44
53.10	102	3.0171	12	11.9937	6.180
70.69	103	1.4006	12	9.9965	22.16
40.29	101	6.7930	12	13.9525	38.17
53.13	102	2.6081	12	11.9896	6.56
70.68	103	1.4242	12	9.9974	28.49
40.16	101	6.8625	12	13.9797	46.32
53.18	102	2.6146	12	11.9842	10.16
70.62	103	1.4182	12	10.003	18.52

Table 9-b. Nb-Ti X-Ray Diffraction Data

Beta-Phase					
<u>2θ</u>	<u>hkl</u>	<u>lorentz-polarization factor</u>	<u>multiplicity factor</u>	<u>structure factor</u>	<u>Intensities</u>
38.88	110	6.8016	12	58.1933	72.39
55.97	200	2.6107	6	50.9756	21.41
70.2	211	1.4301	24	46.0275	28.15
38.90	110	6.7930	12	58.1843	220.1
55.99	200	2.6081	6	50.9679	25.37
70.20	211	1.4242	24	45.9897	44.24
38.74	110	6.8625	12	58.2566	234.6
55.94	200	2.6146	6	50.9872	37.07
70.32	211	1.4182	24	45.9513	65.87
Alpha-Phase					
<u>2θ</u>	<u>hkl</u>	<u>lorentz-polarization factor</u>	<u>multiplicity factor</u>	<u>structure factor</u>	<u>Intensities</u>
39.94	101	6.3623	12	14.0120	14.44
53.10	102	3.0171	12	11.9937	6.180
70.69	103	1.4006	12	9.9965	22.16
40.29	101	6.7930	12	13.9525	38.17
53.13	102	2.6081	12	11.9896	6.56
70.68	103	1.4242	12	9.9974	28.49
40.16	101	6.8625	12	13.9797	46.32
53.18	102	2.6146	12	11.9842	10.16
70.62	103	1.4182	12	10.003	18.52

As we know, two factors influence the position of the phase boundary. One is the alloy composition, as discussed in the *Introduction*. In Nb/Ta-Ti, the β -phase boundary drops to the lower temperature when the β -phase concentration becomes higher in Nb or Ta. In other words, for a fixed alloy composition, increasing the temperature is equivalent to decreasing the Nb/Ta content of β phase boundary. The other factor that affects the β -phase boundary is the interstitial content ^[7]. This might be an important factor, but is not included in this work.

Phase Diagram Calculations by the Regular Solution Model

The calculation of the binary phase diagram based on the regular solution model is expressed using:

$$F^\alpha[x^\alpha, x^\beta, T] = (1-x)F_i^\alpha + xF_j^\alpha + RT[x \ln x + (1-x) \ln(1-x)] + E_{xs}^\alpha \quad (\text{cal/g-atom})$$

Equation 4

Where F^α is the free energy of the α phase, F_i^α and F_j^α are the free energies of the α forms of pure i and j, and E_{xs}^α is the regular solution excess free energy, and can be expressed as $E_{xs}^\alpha = Bx(1-x)$, where B is interaction parameter for bcc phase in the i-j system. The detail is described in Appendix II.

Generally, the interaction parameters are determined by experimental data. In this work, interaction parameters were adopted from Kaufman's ^[11] work for titanium alloys. These parameters from Kaufman together with parameters obtained from Chernov's work ^[26] are listed in Table 10. The calculated phase boundary, as well as some other reference data, is listed in Table 11-a for TaTi and Table 11-b for NbTi binaries respectively.

Table 10. Regular solution parameters for Ti-based stable equilibria

Interaction Parameters	Ti-Ta	Ti-Nb	Sources
<u>Interaction Parameters</u>			
BCC	B=3324	B=3200	[26]
	B=2790	B=3125	[11]
HCP	A=3370	A=3700	[26]
	A=2790	A=3125	[11]
<u>Stability Parameters</u>			
	$\Delta F_{Ti}^{\beta \rightarrow \alpha}(T) = -1050 + 0.91T$		[11]
	$\Delta F_{Nb/Ta}^{\beta \rightarrow \alpha}(T) = 1500 + 0.8T$		[11]

Table 11-a. The tantalum-titanium binary phase boundary

Temperature	Ta wt. % of α -phase boundary	Ta wt. % of β -phase boundary
100° C	<u>0.06^b</u>	<u>99.75^b</u>
200° C	<u>0.79^b</u>	<u>99.14^b</u>
300° C	<u>2.59^b</u>	<u>97.86^b</u>
400 °C	6.94 ^[18] , <u>5.65^b</u>	97.45 ^[26] , 95 ^[18] , <u>95.12^b</u>
450 °C	8.36 ^[18]	<u>91.69^a</u> , 91.7 ^[18]
500 °C	9.8 ^[18] , <u>9.39^b</u>	93.8 ^[26] , <u>82.4^a</u> , 83.4 ^[18] , <u>84.9^b</u>
550 °C	11 ^[18] , 12.15 ^[17]	<u>67.12^a</u> , 74 ^[18]
600 °C	11.87 ^[17] , 11.05 ^[18] , <u>12.8^b</u>	<u>56.94^a</u> , 67 ^[17] , 65.56 ^[16] , 62 ^[18] , 60.69 ^[27] , <u>55.18^b</u>
650 °C	10 ^[18]	48 ^[18] , 61.83 ^[16]
700 °C	10.75 ^[17] , 9.8 ^[18] , <u>13.3^b</u>	50 ^[17] , 58.3 ^[16] , 35.06 ^[26] , 36.5 ^[18] , <u>36.13^b</u>
800 °C	7.97 ^[17] , 5.1 ^[18] , <u>10.79^b</u>	28.9 ^[17] , 43.63 ^[16] , 8.83 ^[26] , 13.5 ^[18] , <u>17.23^b</u>
882.5°C	<u>0.38^b</u>	<u>0.38^b</u>

^a XRD data, ^b predicted data by thermo-cal. All data from this work has been underlined.

Table 11-b. The niobium-titanium binary phase boundary

Temperature	Nb wt. % of α -phase boundary	Nb wt. % of β -phase boundary
100° C	<u>0.25^b</u>	<u>99.7^b</u>
200° C	<u>0.95^b</u>	<u>98.9^b</u>
300° C	<u>2.23^b</u>	<u>97.21^b</u>
375 °C		60 ^[19]
380 °C		37 ^[20] , 63 ^[21,35] , 55.95 ^[18]
400 °C	4.11 ^[18] , <u>4.01^b</u>	54.95 ^[18] , <u>93.95^b</u>
420 °C		58 ^[42] , 62 ^[23] , 64 ^[41]
450 °C	4.39 ^[18]	<u>85.75^a</u> , 46.47 ^[18]
500 °C	4.39 ^[18] , <u>6.01^b</u>	<u>72.19^a</u> , 40 ^[18] , <u>86.37^b</u>
550 °C	4.25 ^[18]	<u>60.6^a</u> , 33.0 ^[18]
600 °C	4.1 ^[18] , <u>6.99^b</u>	28.05 ^[18] , <u>41.73^b</u>
650 °C	3.68 ^[18] ,	22.8 ^[18]
680 °C		32.67 ^[8]
700 °C	3.1 ^[18] , <u>5.7^b</u>	15.5 ^[18] , <u>23.02^b</u>
725 °C		25.51 ^[8]
765 °C		17.74 ^[8]
800 °C	1.42 ^[18] , <u>3.0^b</u>	6.2 ^[18] , <u>9.73^b</u>
810 °C		9.27 ^[8]
882.5° C	<u>0.19^b</u>	
885 °C		0 ^[8]

^a XRD data, ^b predicted data by thermo-cal. All data from this work has been underlined.

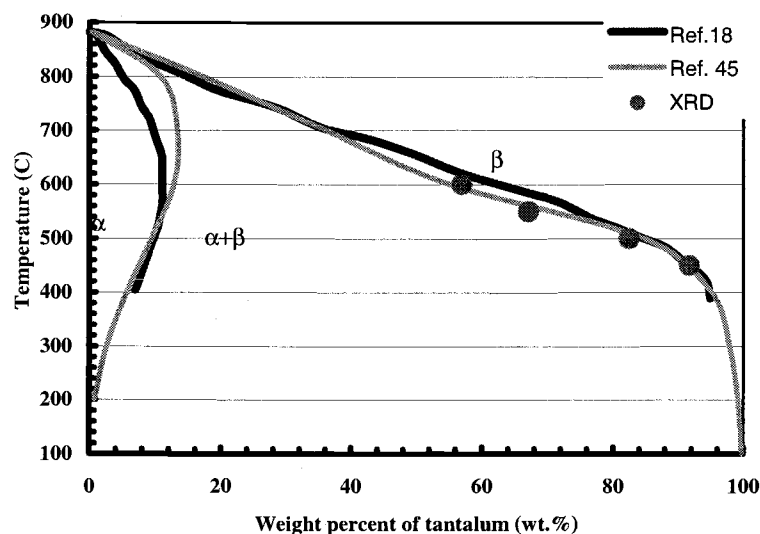


Figure 7. The binary Ta-Ti alloy system at low temperatures. The solid thick lines indicate the standard binary phase diagram^[18]. The solid thin lines show the calculated phase boundaries from the regular solution model calculations. The circles show the XRD results from this work.

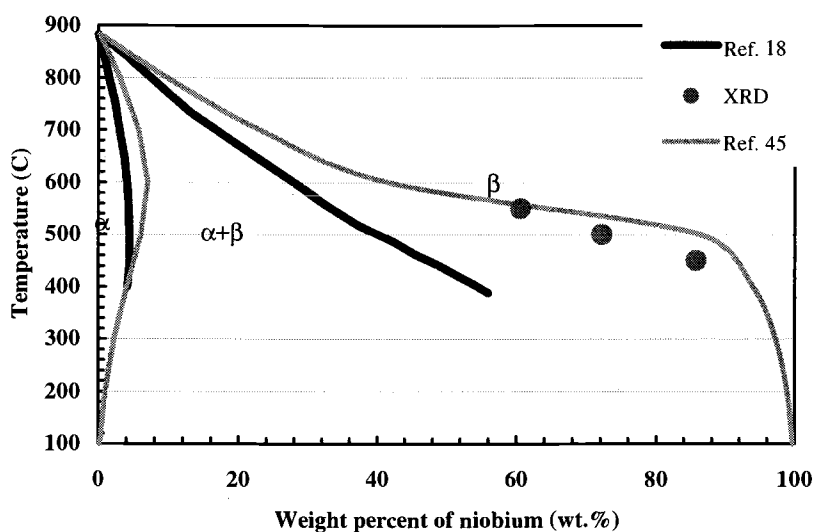


Figure 8. The binary Nb-Ti alloy system at low temperatures. The black lines indicate the standard binary phase diagram^[18]. The grey lines show the calculated phase boundaries from the regular solution model calculations. The circles show the XRD results from this work.

In TaTi binary system, our XRD data agrees with our predicted β -phase boundaries, as well as to the published one at a temperature $< 500^\circ\text{C}$ and $> 700^\circ\text{C}$ very well, see Figure 7. But end up with a lower tantalum content for beta phase than ASM data at 550°C and 600°C . The calculation, as well as all experimental data from the literature of beta-phase boundaries is shown in Table 11.

As we mentioned before, thermo-calculation allows us to extend our work to where the experiment couldn't reach. The β phase boundaries of Ta-Ti and Nb-Ti binary systems are thermodynamically predicted at all temperatures and compositions. There are only two sets of data for Ta-Ti at temperatures lower than 450°C . Both works approach this issue by using the regular solution model. One is from Chernov's work ^[26], and the other one is from this work. The difference of our results and Chernov's is very small at low temperature. However, our results at 450°C and 500°C are closer to both XRD ones and the published ones than Chernov's.

The stability parameters and interaction parameters can be determined by the presence of positive values of the excess thermodynamic potential E_{xs} , which correspond to the last term in equation (4), whose numerical characteristic is the value of the interaction parameter in the phase considered, details are explained in Appendix II. The positive values of the parameters are indicative of the tendency of these systems to demixing. Chernov's ^[26] results, as shown in Table 10, are similar to the data from Kaufman ^[11]. However, Chernov uses larger interaction parameters and a difference between β -phase and α -phase interaction parameters. This is why their results have a higher tantalum content β -phase boundary at 400°C and 500°C , and a smaller tantalum content β -phase boundary at 800°C . Larger positive interaction parameters always show wider two-phase fields. But their results agree with the published data at 600°C and 700°C pretty well, and the discrepancy is less than 1%.

Contamination Effect

As we mentioned in the *Introduction*, Summer's and Maykuth's β -phase boundaries have much higher Ta content than all other works. The reason is the most possible due to the contamination.

No experiments have been carried out to determine the extent of the solubility of Ta/Nb in α -Ti. Our β -phase boundary of Nb-Ti binary that is predicted by the regular solution model and XRD results has a higher Ta solubility at higher temperature than ASM^[18]. No experiments have been carried out on the effect of contamination in determining the β -phase boundary. However, a lot of effort has been put on clean sample preparation in order to get rid of the contamination. Following are the facts that imply our β -phase boundary is not due to the contamination:

1. The Nb-Ti and Ta-Ti binary samples are under same heat treatment conditions. Ta-Ti binary phase diagram shows a good agreement with ASM standard, as well as to all other references. So, our Ta-Ti is free from contamination, same as Nb-Ti samples.
2. All samples without Ar back-filled shows the oxygen layer, even at low temperature (400°C). However, not a single sample under Ar back-filling shows the oxygen layer, even at high temperatures, such as 600°C

Kinetics of β and α Transformations

The kinetics must be considered when evaluating the experimental phase diagram data. In an alloy like TaTi, the diffusion coefficient of interest is the interdiffusion coefficient. The diffusion coefficient of the TaTi system was measured by Ansel^[46] using TaTi diffusion couples and Ta/TaTi pellet. The data was collected over a temperature range of 1000°C to 1900°C. The interdiffusion coefficients were calculated from concentration

profiles determined by EMPA. There are several characteristics about TaTi diffusion ^[47], and they are summarized as follows:

- a. In the same way as other Ti alloys, the diffusion coefficient increases exponentially with increasing temperatures and decreasing β -stabilizer (tantalum) content.
- b. The Arrhenius plot of $\ln D$ vs $1/T$ does not give a straight line, but curved. At low composition, the plot has a disperse trend with decreasing the temperature, and D and Q increase with Ta content. By using $D = D_0 \exp(-Q/RT)$ to fit the data, the activation energy and frequency factors have a maxima around 35 at % to 40 at % of Ta ^[46]. The Arrhenius plot converges after 35 at % with decreasing the temperature, and D_0 and Q decrease with tantalum content. The discontinuity (around 35 at %) is considered as a change of the diffusion mechanism, called the crossover point. Before this point (35% composition), one diffusion mechanism dominates the diffusion system, but it doesn't mean there is only one diffusion mechanism operating.

Over the whole range, there may be two or more diffusion mechanisms existing. The curvature of the Arrhenius plot suggests an increase in the activation energy and frequency factors with temperature. Therefore neither D_0 nor Q are constant. According to these characteristics, it will be more reasonable to consider two or more diffusion mechanisms in this system, instead of fitting all data into one equation over such wide composition and temperature ranges. For refractory alloys, a suggested ^[48] two diffusion mechanism model is proposed as follows:

$$D = D_1 + D_2 \quad \text{Equation 5}$$

where

$$D_1 = D_{01} \exp(-Q_1/RT),$$

$$D_2 = D_{02} \exp(-Q_2/RT),$$

D is interdiffusion coefficient, in the unit of cm^2/s , D_{01} and Q_1 versus D_{02} and Q_2 represent the different diffusion mechanisms, and this will be discussed further later. Here, the D_0 is in the unit of cm^2/s and Q is in the unit of J.

We consider this transition point as the separation point for different diffusion mechanisms, and obtain D_{01} , Q_1 , D_{02} , Q_2 as follows:

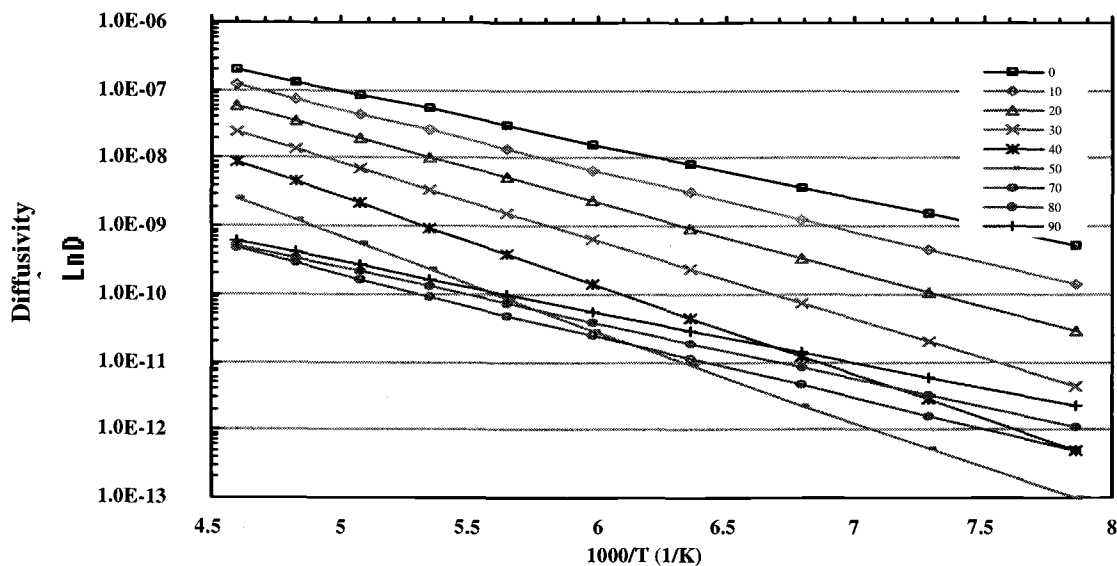


Figure 9. Semilog plot of the diffusivity as a function of the inverse of the temperature for Ta-Ti binary alloy. The lines show diffusivity at different compositions (weight percentage).

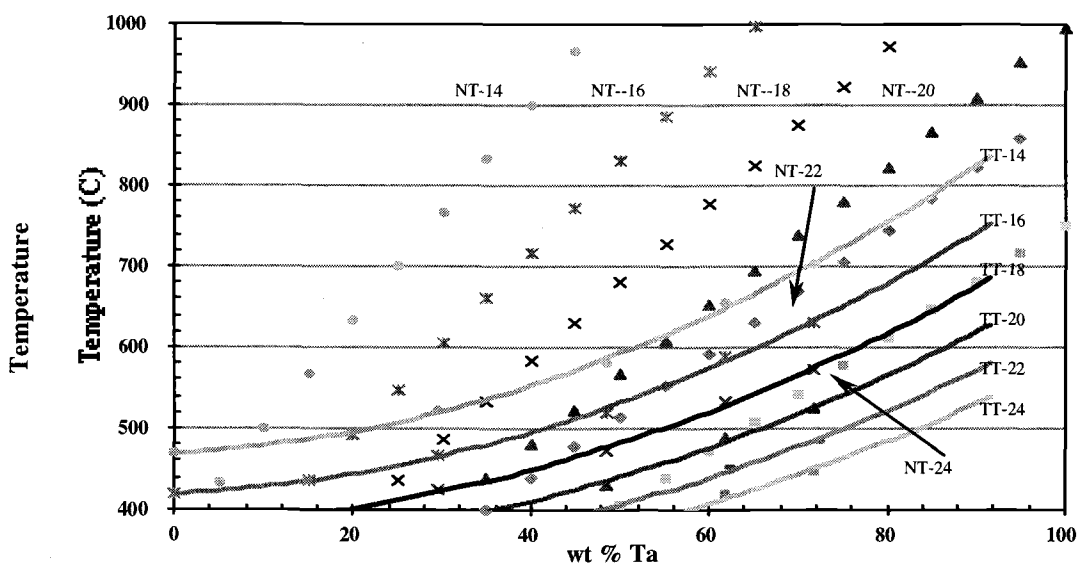


Figure 10. Comparison of interdiffusion coefficients of Nb-Ti and Ta-Ti binary systems. The Ta-Ti diffusivity (in the unit of cm^2/s) is higher than that in Nb-Ti binary at same temperature and compositions. At 550 °C, our Ta-Ti samples (50 wt.% Ta) is around 5 order of magnitude higher than that of Nb-Ti (53 wt.% Nb) binary.

$$D_{01} = 9E-4 * \exp(0.0575 * x) \text{ [cm}^2\text{/s]}, Q_1 = 36238 * \exp(0.0125 * x) \text{ (} 0 < x < 30 \text{)}$$

$$D_{02} = 4E-4 * \exp^{(-0.0612 * x)}, Q_2 = 78063 * \exp(-0.0092 * x) \text{ (} 35 < x < 90 \text{)}$$

The modified Arrhenius plot of $\ln D$ vs. $1000/T$, as shown in Figure 9, is a group of straight lines. This indicates a better fit by using two-diffusion-mechanism model. The diffusion rate of Ta-Ti and Nb-Ti are compared in Figure 10. Nb-Ti data is taken from Moffat's thesis ^[7]. The Ta-Ti system has three or four orders of magnitude higher diffusion rate than that of Nb-Ti. For instance, the diffusivity of Nb47Ti at 450°C is about $1E-21 \text{ m}^2\text{/s}$, and about $1E-18 \text{ cm}^2\text{/s}$ in Ta47Ti. The diffusion rate of Nb47Ti and Ta47Ti at 550°C is $1E-20 \text{ cm}^2\text{/s}$ and $1E-16 \text{ cm}^2\text{/s}$. This means that if Ta-Ti can reach the equilibrium state at 450°C in 24 hours, it probably will take 1000 days for the Nb-Ti system to reach the equilibrium state. This is why we have clearly defined Ta-Ti α -phase peaks, but not in NbTi at the same annealing conditions.

Conclusions: For Ta-Ti binary alloy, our experiment data, theoretically predicted β -phase boundaries are very close to ASM published data, as well as to the most of the reference data. However, both our experimental data and theoretical predicted data in Ta-Ti binary alloy show an obvious higher β -phase boundary than ASM published results. However, our experimental data and our predicted results are self-consistent.

Ternary Alloy Systems

The Nb-Ti-Ta ternary alloy phase diagrams are determined using regular solution model calculation and XRD, and the final phase diagram is extrapolated according to experimental results.

Ternary samples and Adopted Model

Figure 10 shows a ternary phase diagram and the six as received ternary samples investigated. Comparing this diagram with Figure two in the *INTRODUCTION*, it is not

hard to see that out of six ternary samples, only two of them (Nb₂₈Ta₄₁Ti and Nb₂₄Ta₄₉Ti) can really be driven to the high H_{c2} after heat treatment. The As-received samples are distributed all around the H_{c2} peak (around 400 °C to 600°C). Only if β -phase is in convex shape, all samples will be in the $\alpha+\beta$ two phase region, and will be useful to do phase analysis under all precipitate temperatures.

Ternary Alloy Phase Diagrams

Thermo-Calculation phase Diagrams

The ternary phase diagram predicted by first principle calculation based on the regular solution model that is described in detail in Appendix II is displayed in Figure 11. At all temperatures, the β phase boundaries are in concave shape, as expected before ^[1].

However, a smaller $\alpha+\beta$ intermediate phase region is resulted. One thing that needs to be mentioned is that in the ternary alloy system, more assumptions were made in the calculation due to its more complicated interactions, and it is therefore much more uncertain.

X-Ray Diffraction Results

Evaluation of the ternary phase diagram according to the XRD is shown in Figure 12. From Figure 12, we can see that the phase boundaries at different temperatures have different shapes. The 550°C one is more convex and 400 °C one is more concave in shape. The 400°C one is nearly lying on top of the 450°C one. When diffusion kinetics are considered, there is about four orders of magnitude difference of diffusivity between these two temperatures. This strongly suggests an insufficient heat treatment time used for 400°C. A rough estimation of the heat treatment time used for 400°C to reach equilibrium is about 10,000 times longer than that used for 550°C. Therefore, the 550°C

XRD data is more reliable to represent the phase boundary. Based on the 550°C data, an extrapolated ternary phase diagram is therefore built, as shown in Figure 13.

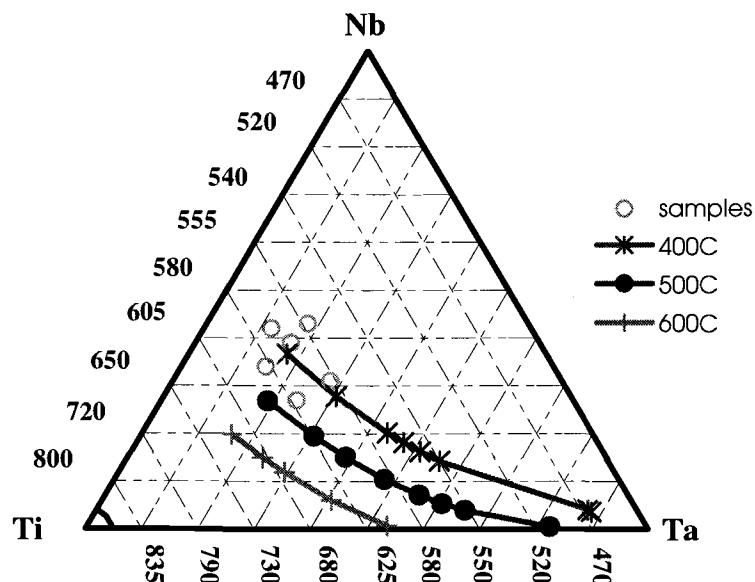


Figure 11. Type B ternary phase diagram and investigated samples which showing the starting alloy compositions studied in this work (empty circles) and the calculated β -phase boundary at 400, 500, and 600 °C using regular solution model.

Table 12-a. The niobium-titanium-tantalum ternary β -phase boundary-XRD

Starting alloy	NbTiTa wt. % of β -phase composition				
	400°C	450°C	500°C	550°C	600°C
1246		3329		1535	
1551				2139	
1774	2422			1936	
1839	2921			2129	
2449	2038				
2841	1939				

Table 12-b. The niobium-titanium-tantalum ternary β -phase boundary-Calculation

NbTaTi wt. % of β -phase composition		
400°C	500°C	600°C
88.09Ta8.27Ti	18.91Ta54.22Ti	15.98Ta64.13Ti
87.26Ta8.75Ti	30.85Ta49.64Ti	24.07Ta60.9Ti
55.7Ta29.95Ti	38.69Ta46.21Ti	29.49Ta58.56Ti
51.32Ta32.38Ti	47.93Ta41.59Ti	40.74Ta53.16Ti
47.33Ta34.43Ti	55.77Ta37.08Ti	53.29Ta46.01Ti
43.43Ta36.3Ti	60.66Ta33.95Ti	
30.65Ta41.57Ti	65.43Ta30.64Ti	
17.44Ta45.9Ti	82.26Ta17.27Ti	

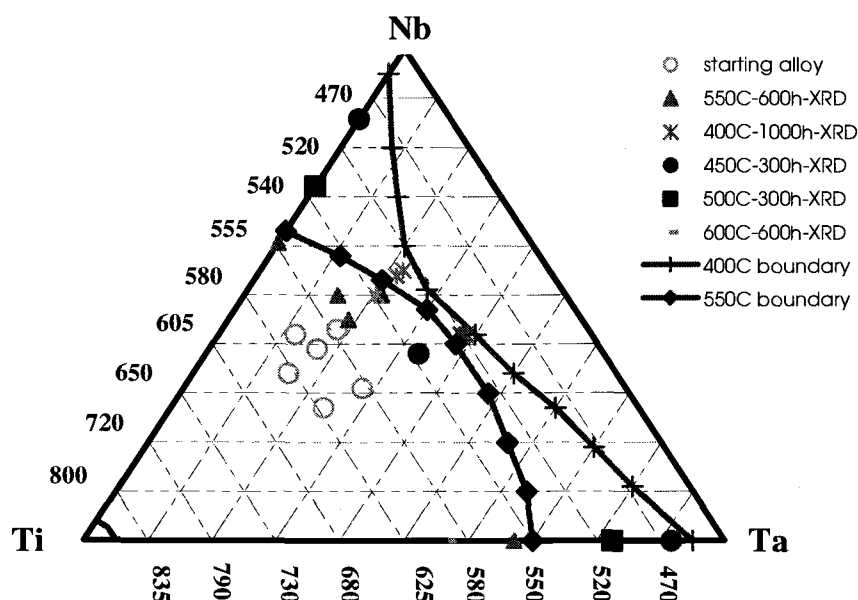


Figure 12. Experimental data from precipitating heat treatment at different temperatures in Nb-Ti-Ta ternary alloy system. The hollow circles are as-received samples. All others are XRD data from different treatment temperature and times. Notice there are some overlaps for 550°C data and 450°C data.

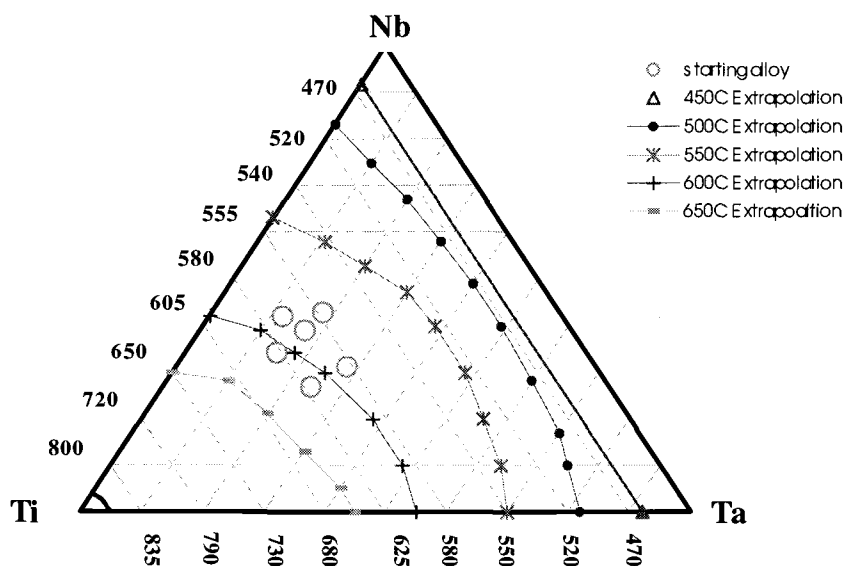


Figure 13. The extrapolated ternary equilibrium phase diagram for the Nb-Ti-Ta system. The dotted lines mark the extrapolated position of the β -phase boundary at 450, 500, 600, and 650°C. The solid line at 550°C is the experimentally determined β -phase boundary from the quantitative XRD analysis. The solid line near the Ti apex is the approximate α -phase boundary. For this work, the assumption was made that the α -phase boundary was independent of temperature.

Diffusion Behavior of Ternary Alloys

The diffusion rates of Nb-Ti-Ta ternary at different temperatures are estimated based on the binary data, and are shown in Figure 14-16. At 400°C, the β phase boundary is located below diffusion coefficients of $1\text{E-}20\text{ cm}^2/\text{s}$, and has diffusivity of about $1\text{E-}21\text{ cm}^2/\text{s}$. At 500°C, all samples are within the range of $1\text{E-}20\text{ cm}^2/\text{s}$ to $1\text{E-}18\text{ cm}^2/\text{s}$. From these diffusion plots, a heat treatment time and precipitate size can be estimated. Compared with similar composition of binary samples, the diffusion rate of ternary samples (Nb51Ti15Ta and Nb49Ti24Ta) at 400°C are very close to that in TaTi. The α -precipitate size after the heat treatment is estimated to be about 100 nm in diameter in ternary alloy system. The α -precipitate size is about 3 to 5 times larger than that in the Ta50Ti binary system based on the estimation from diffusion length $X=\sqrt{Dt}$.

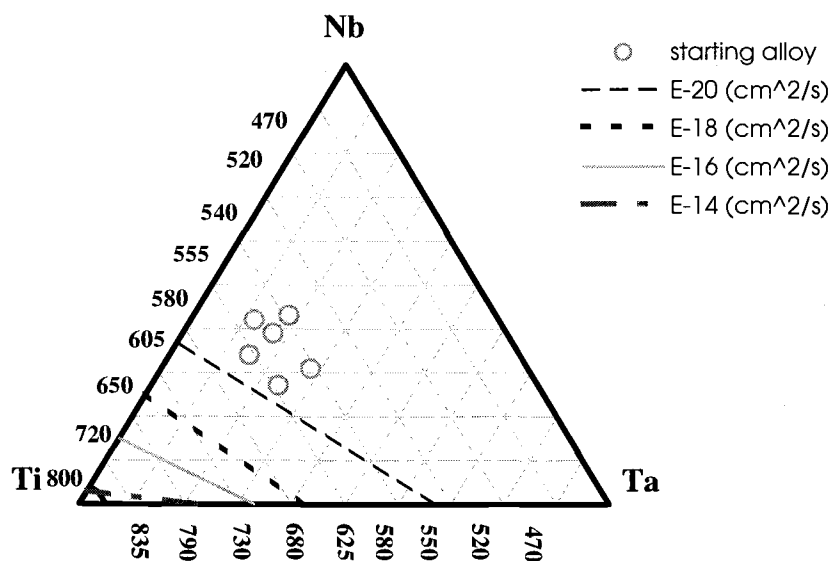


Figure 14. Ternary diffusivity-Lines of constant diffusivity plotted on the Nb-Ti-Ta ternary phase diagram at a temperature 400°C. The inter-diffusivity coefficient extends over a range from 10^{-14} – 10^{-20} cm²/s.

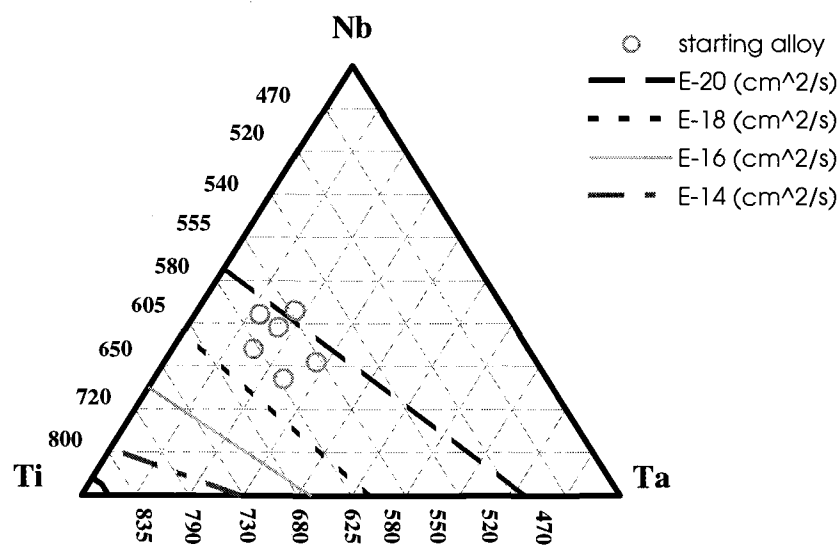


Figure 15. Ternary diffusivity-Lines of constant diffusivity plotted on the Nb-Ti-Ta ternary phase diagram at a temperature 500°C. The inter-diffusivity coefficient extends

over a range from 10^{-14} – 10^{-20} cm²s.

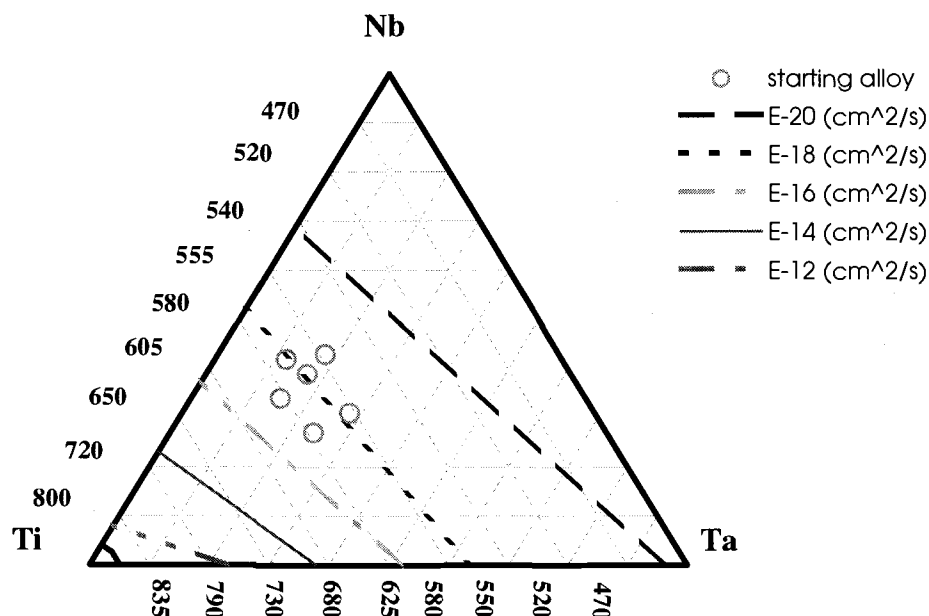


Figure 16. Ternary diffusivity- Lines of constant diffusivity plotted on the Nb-Ti-Ta ternary phase diagram at a temperature 600°C. The inter-diffusivity coefficient extends over a range from 10^{-12} – 10^{-20} cm²/s.

Critical Temperature For Binary and Ternary Alloy Systems

Critical temperature measurements were carried out by an inductive method.

Temperatures were measured by Cernox RTD thermometer with 0.005 precision.

Inductive measurements were implemented at a frequency of 500 Hz. Generally speaking, the resistively measured T_c values are higher than inductively measured ones, although both follow a similar trend. The resistive method probes the best one dimensional superconducting path, whereas the inductive method provides more of a volume average of T_c transitions. Resistive transitions are about 0.1 K wide according to Suenaga, inductive transitions are around 0.35K, or even more in our case.

Other effects that may influence T_c are the annealing time and annealing temperature.

The higher the annealing temperature and the longer the annealing time, the higher the

transition width of T_c , as shown in Appendix III. The increment of transition width with aging time is attributed to niobium enrichment of the matrix that accompanies the α -Ti precipitation and incomplete diffusion in the β -phase.

The measured critical temperatures of fifty-eight samples are listed in the table in Appendix III. The critical temperatures vary from 6.65 K for As-Received Ta50Ti to 10.77K for Nb55Ti heat treated at 500C for 112 hours, and the transition width varies from 0.04 K to 1.94 K. Some of our transitions are really wide compared with Suenaga's data. Especially for Nb46Ti12Ta ternary samples, the average width of this composition of eight samples is 1.22 K. The reason for that is not clear yet. Our other four ternary samples have a very good homogeneity according to the EMPA results though.

Our T_c data is plotted on top of Suenaga's plot, converted to weight percentage of compositions, as shown in Figure 17. The transition temperatures of α -Ti or martensite α'' phase are low, and observed T_c for any given alloy depends not on the average composition of alloy but on T_c of highest T_c phase present, the BCC- β phase. It is noticed that the T_c data for 400 °C-1000hrs is less valuable. Although they are under the longer annealing time, the kinetics of these ternary samples depends on temperature more than time, as we discussed before. Therefore, the T_c data at 400 °C is less reliable.

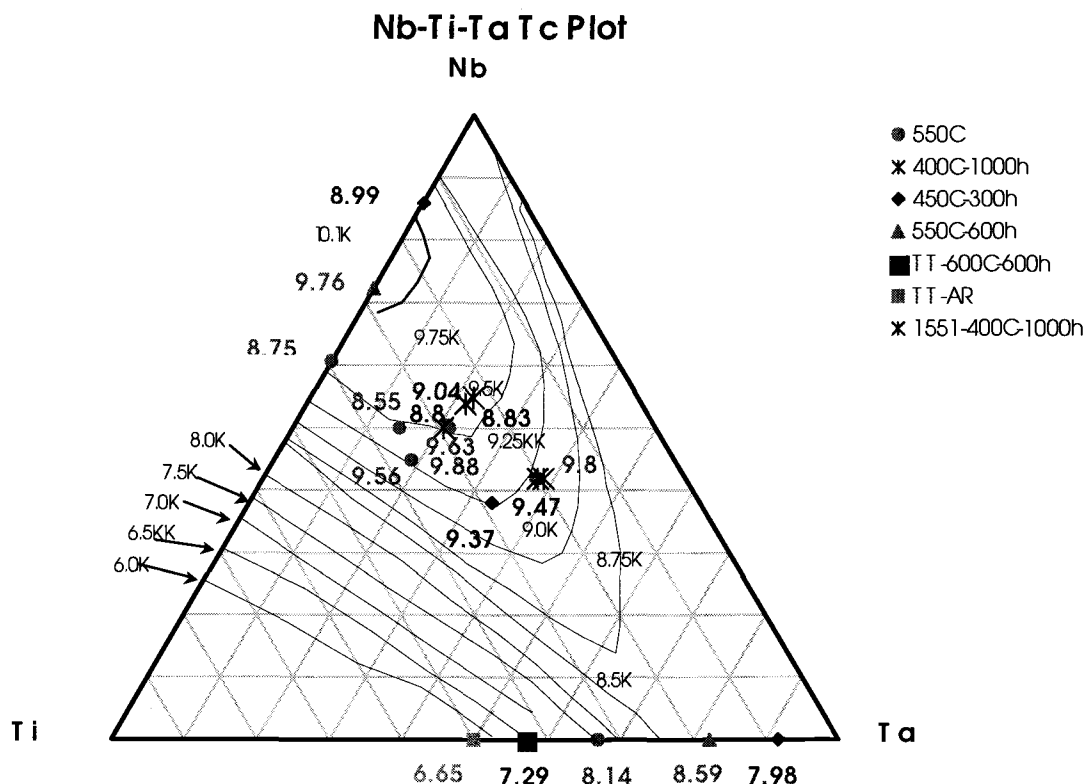


Figure 17. Critical temperature as a function of alloy compositions. The lines represent the data of Suenaga and Ralls^[30], while the data points indicate the measurements of this work. The compositions given are composition of β -phase for heat treated alloys.

Conclusions:

From the detailed study of metallurgy of Nb-Ti-Ta ternary and its binary systems, following conclusions are drawn:

1. A working ternary equilibrium phase diagram for the Nb-Ti-Ta system has been developed that is based on experimental measurements and quantitative thermodynamic calculations. The ternary phase diagram can be used as a metallurgical tool for ternary alloy development and design of ternary alloy processing.
2. Evaluations of the thermodynamics and XRD measurements of the Nb-Ti and Ta-Ti binary systems have led to improved versions of the equilibrium binary phase diagrams. In particular, the Nb-Ti phase diagram developed here shows the

β -phase boundary at higher temperatures and lower Ti compositions than the presently accepted phase diagram.

3. Measurements of the superconducting critical temperature, T_C , show good agreement with previous measurements of T_C in the ternary alloys. Changes to the T_C as a function of precipitation heat treatments cause the T_C to follow the composition changes in the β -phase as Ti precipitation occurs. In the alloys and heat treatments studied here, the T_C remained above 8K, which should result in minimal impact on applications for the ternary alloys in magnet systems.
4. Coupled with previous information on the expected H_{C2} behavior of the ternary alloys, the phase diagram and T_C data indicate that there is still reason to expect the Nb-Ti-Ta ternary system is capable of reasonable properties for high field magnet applications at temperatures below 4.2K.

BIBLIOGRAPHY

- 1 W. H. Warnes and N. Li, Adv. Cryogenic Engr., 46:923-930 (2000).
- 2 W. H. Warnes and N. Li, -A Continuation Final Report, final report submitted to Fermi National Accelerator Laboratory, (September, 2000).
- 3 Joint Committee on Powder Diffraction Standards (JCPDS)-International Center for Diffraction Data (1998).
- 4 E. K. Molchanova, Phase Diagrams of Titanium Alloys. Jerusalem, Israel Program for Scientific Translations, D. (Davey, New York.1965).
- 5 P. J. Lee, Encyclopedia of Electrical and Electronics Engineering, 21:75-87, New York: John Wiley & Son, Inc., (1999)
- 6 B. D. Cullity, Elements of X-Ray Diffraction, Addison-Wesley Publishing Company, Inc. Reading, Massachusetts (1978).
- 7 D. L. Moffat, Ph.D Thesis University of Wisconsin, Madison, (1985).
- 8 M. Hansen, E.L. Kamen, H. D. Kessler, and D. J. McPherson, Trans. AIME, J. Metals, October: 881-888 (1951).
- 9 Brown, A. R. G., Clark, D. Eastabrook, J. and Jepson, K. S. Nature, 210:914-915 (1964)
- 10 J. L. Murray, Phase Diagrams of Binary Titanium Alloys, ASM, Metals Park, OH (1987)
- 11 Kaufman, L. and Bernstein, H., Computer Calculations of Phase Diagrams, Academic Press, New York (1970).
- 12 Imgram, A. G., Williams, D. N., Wood, R.A., Ogden, H. R., and Jaffee R. I. , WADC Tech Rept (Wright Air Development Center. Technical Report):59-595, Part II (1961).
- 13 Ronami, G. N., Kuznetsova, S. M., Fedotov, S. G. and Konstantinov, K. M. Moscow Univ Phys Bull, 25(2): 55-57 (1970)
- 14 R. Krishnan, S. P. Garg, N. Krishnamurthy & E. Paul, Journal of Alloy Phase Digrams, 3 (1):28-30 (1987).
- 15 D. S. Summer. Journal of Institute of Metals. 81: 73 (1952-1953).
- 16 D. S. Summer, Journal of Institute of Metals. 81:426 (1952-1953).

- 17 D. J. Maykuth, H. R. Ogden, R. I. Jaffee, J. of Metals. February : 231 (1953).
- 18 T. Massalski, ed., Binary Alloy Phase Diagrams, ASM International, Metals Park, OH (1990).
- 19 Liu H. and E. Gregory, K.J. Faase, and W.H. Warnes, "*Development of Multifilamentary Superconductors Containing Nb-41WT%Ti28WT%Ta Ternary Alloys*", Adv. Cryogenic Engr., Kluwer Academy Publisher, New York, 42:1135-1142 (1996).
- 20 M. Panek, D. Oattanayak, R. Meier-Hirner, and H. Kupfer, J. Appl. Phys., 54(12), (December):7083-7088 (1983).
- 21 R. Taillard, E. Florianova, C. E. Bruzek, and G. K. Hoang, Adv. Cryogenic Engr., 42:1151-1158 (1996).
- 22 G. K. Hoang, C. E. Bruzek, L. Oberli, and D. Leroy, 1995, IEEE Trans. Appl. Superconductivity, 5(2), (June):412-415 (1995).
- 23 P. J. Lee, J. C. McKinnell, and D.C. Larbalestier, Adv. Cryogenic Engr., Kluwer Academy Publisher, New York, 38:691-697 (1992).
- 24 P. J. Lee, C.M. Fischer, D.C. Larbalestier, M.T. Naus, A. A. Squitieri, W. L. Starch, R. J. Werner, P.J. Limon, G. Sabbi, A. Zlobin, E. Grogory, IEEE Trans. Appl. Superconductivity, 9(2):1571-1574 (1999).
- 25 P. J. Lee, D.C. Larbalestier, J. C. Mckinnell, and A. D. McInturff, IEEE Trans. Appl. Superconductivity, 3(1), (March):1354-1357
- 26 D. B. Chernov, et al., Titanium and Titanium Alloys. Plenum AIME. New York 2:1307 (1976).
- 27 T. Sasaki, K. Noto, and Y. Muto, Jap. J. Appl. Phys., 24(6):679-681(1985).
- 28 H. Wada and K. Tachikawa, T. Kato, IEEE Trans. Magn., MAG-17 (1):61-64 (1981).
- 29 M. Wake, T. Shintomi, M. Kobayashi, K. Tsuchiya, H. Hirabayashi, H. Wada, K. Inoue, K. Itoh, K. Tachikawa, K. Ishibashi, and A. D. McInturff, IEEE Trans. Magnetics, MAG-19 (3), (May):552-555 (1983).
- 30 M. Suenaga and K. M. Ralls, J. Appl. Phys., 40 (11), (October):4457-4463 (1969).
- 31 D. G. Hawsworth and D.C. Larbalestier, IEEE Trans. Magn., MAG-17 (1):49-52 (1981).

- 32 D. G. Hawksworth and D.C. Larbalestier, Adv. Cryogenic Engr., Kluwer Academy Publisher, New York, 26:479-486 (1980).
- 33 N. Zhou, X. Z. Wu, Y. P. Li, Y.C. Yie, and L. Zhou, 1988, Adv. Cryogenic Engr., Kluwer Academy Publisher, New York,, 34:995-999 (1988).
- 34 L.V. Potanina, G. P. Vedernikov, V. Yu. Korpusov, A.D. Nikulin, S. I. Novikov, and M. S. Novikov, Adv. Cryogenic Engr., Kluwer Academy Publisher, New York, (Materials), 44:881-887 (1998).
- 35 G. P. Vedernikov, L.V. Potanina, V. Yu. Korpusov, V.A. Drobishev, V.S. Zurabov, A.S. Zolotarjev, A.D. Nikulin, N.I. Kozlenkova, and S. I. Novikov, IEEE Trans. Appl. Superconductivity, 7(2), (June):1751-1754 (1997).
- 36 H. R. Segal, T. A. de Winter, Z. J. J. Stekly, and K. Hemachalam, IEEE Trans. Magn, MAG-17 (1), (January):53-56 (1981).
- 37 D.C. Larbalestier, Superconductor Materials Science, Plenum Press, New York and London (1981).
- 38 J. C. McKinnell, P.J. Lee, R. Resmbottom, D.C. Larbalastier, P. M. O'Larey, and W.K. McDonald, Adv. Cryogenic Engr., Kluwer Academy Publisher, New York,34:1001-1007 (1988).
- 39 H. R. Segal, Z. J. J. Stekly, and A. de Winter, IEEE Trans. Magn., Mag-17 (5), (September):1645-1648 (1981).
- 40 D.C. Larbalestier, Adv. Cryogenic Engr., 26:10-36 (1980).
- 41 Liu H. and E. Gregory, 1992, IEEE Trans. Appl. Superconductivity, 3(1):1350-1353 (1992).
- 42 E. Gregory and T. Pyon, IEEE Trans. Appl. Superconductivity, 9(2):1567-1570 (1999).
- 43 T. Shimada, K. Wada, S. Meguro, S. Murase, S. Nakayama, T. Orikasa, K. Makishima, K. Watanabe, K. Tsuchiya, A. Yamamoto, T. Nakamoto, and T. P. Shintomi, IEEE Trans. Appl. Superconductivity, 9(2):1731-1734 (1999).
- 44 L.V. Potanina, G. P. Vedernikov, A. K. Shikov, V. Yu. Korpusov, S. V. Scherbakov, S. I. Novikov, M. S. Novikov, Adv. Cryogenic Engr., Kluwer Academy Publisher, New York, 46(B):939 (2000)
- 45 L. Na and W. H. Warnes, IEEE Trans. Appl. Supercond., 11(1):3800-3803, (March 2001).

- 46 Ansel, I. Thibon, M. Bolivean and J. Debuigne, *Acta metall.* 46(2) (1998) 423-430
- 47 G. Rajesh and S. V. Varamban, *CALPHAD*, 21(4):509-519 (1997).
- 48 I. Ansara, *Alloy Phase Diagrams*, 19:107-114 (1983).

APPENDICES

Appendix I XRD Analysis Routine

If a sample contains n-phases, the intensity I_n diffracted by the i th phase is proportional to the quantity of that phase present in the alloy. Intensity of the diffracted beam from a single phase powder specimen containing randomly oriented grains in the form of a flat plate in a diffractometer was first worked out by J. J. Thomson and modified later as follows:

$$I = \left(\frac{I_0 A \lambda^3}{32\pi r} \right) \left[\left(\frac{\mu_0}{4\pi} \right)^2 \frac{e^4}{m^2} \right] \left[\left(\frac{1}{v^2} \right) \right] \left[F^2 P \left(\frac{1 + \cos^2 2\theta}{\sin^2 \theta \cos \theta} \right) \right] \left(e^{-2M} \right) \left(\frac{1}{2\mu} \right) \quad \text{Equation A1}$$

I: integrated intensity of diffraction peak

I_0 : incident beam intensity

A: incident beam cross section area

λ : incident beam wavelength

r: radius of the diffractometer circle

μ_0 : constant, $4\pi \times 10^{-7} \text{ m kg C}^{-2}$

e: electron charge

m: electron mass

v: unit-cell volume

F: structure factor

P: multiplicity factor

θ : Bragg angle

e^{-2M} : temperature factor

μ : linear absorption coefficient

Rewrite equation A1 as: $I = \frac{KR}{2\mu_{\text{alloy}}}$ Equation A2

where: $\left(\frac{\mu}{\rho} \right)_{\text{alloy}} = w_1 \left(\frac{\mu}{\rho} \right)_1 + w_2 \left(\frac{\mu}{\rho} \right)_2 + \dots$ Equation A3

$$K = \frac{I_0 A \lambda^3}{32\pi r} \left[\left(\frac{\mu_0}{4\pi} \right)^2 \frac{e^4}{m^2} \right]$$

$$R = \frac{1}{V^2} \left[F^2 p \left(\frac{1 + \cos^2 2\theta}{\sin^2 \theta \cos \theta} \right) \right] e^{-2M}$$

K is the first two terms of equation A1, and is independent of diffraction materials, and therefore being considered as a constant. R is combination of the third, the fourth and the fifth terms of the equation A1. R, depends on the nature of the phase, diffraction angle (θ) and hkl.

Notice that the equation A1 is true only for the single-phase alloy. When calculating an intensity of reflection from one phase out of a mixture of phases, we multiply the right hand side of equation A1 by C_α , the volume fraction of the α -phase in the alloy.

Manipulating Equation A1, A2 and taking account of the volume fraction factor C_α , the intensity of a reflection of the α -phase can then be written as

$$I_\alpha = \frac{K_2 R_\alpha C_\alpha}{2\mu_{\text{alloy}}} \quad \text{Equation A4.1}$$

$$I_\beta = \frac{K_2 R_\beta C_\beta}{2\mu_{\text{alloy}}} \quad \text{Equation A4.2}$$

So, the volume fraction ratio of two phases is:

$$\frac{C_\alpha}{C_\beta} = \frac{R_\beta I_\alpha}{R_\alpha I_\beta} \quad \text{Equation A5.1}$$

$$C_\alpha + C_\beta = 1 \quad \text{Equation A5.2}$$

R can be worked out from XRD results, described in details in the follows. Combining equation A5.1 and A5.2, the volume fraction of each phase can be obtained.

Determination of R value:

In order to know the proportion of each phase, we need to know the integrated intensity ratio of the two phases and the R ratio of the two phases. The integrated intensities are obtained from the XRD experiment. R-values are obtained from the following procedures.

$$R = \left(\frac{1}{v^2} \right) \left[F^2 P \left(\frac{1 + \cos^2 2\theta_B}{\sin^2 \theta_B \cos \theta_B} \right) \right]$$

Here we ignore the temperature effect because all we run is in a constant (room temperature) condition.

$v = a^3$ for BCC

$v = 0.866 a^2 c$ for Hexagonal

Multiplicity Factor (P)

Table A1 Multiplicity factors ^[6]

HCP (alpha-Ti)		BCC (beta-Nb,Ta)	
hkl	P	hkl	P
002	6	110	12
101	12	200	6
102	12	211	24
103	12	220	12

Lorentz-Polarization Factor (LPF)

The overall effect of this geometrical factor is to decrease the intensity of reflection of θ , and is described as:

$$\frac{1 + \cos^2 2\theta}{\sin^2 \theta \cos \theta}$$

Structure Factor

$$\text{BCC: } F = f e^{2\pi i(0)} + f e^{2\pi i(h/2+k/2+l/2)} = f [1 + e^{\pi i(h+k+l)}]$$

$$F = 2f, \quad h+k+l = \text{even};$$

$$F = 0, \quad h+k+l = \text{odd}.$$

$$\text{HCP: } F = f [1 + e^{2\pi i\{(h+2k)/3+l/2\}}];$$

Atomic Scattering Factor (ASF)

ASF is used to describe the “efficiency” of scattering of a given atom in a given direction. The atomic scattering factor data was taken from reference^[6], and then plotted in Excel. The best fit is derived from the plot and shown in the following equations.

$$ASF_{Ti}=21.03-18.815x-142.06x^2+538.41x^3-796.31x^4+541.25x^5-139.53x^6$$

$$ASF_{Nb}=41.041-16.559x-295.74x^2+972.9x^3-1348.4x^4+876.99x^5-218.65x^6$$

$$ASF_{Ta}=73.017-24.878x-379.19x^2+1094.1x^3-1349x^4+789.21x^5-178.66x^6$$

$$ASF_{\beta}=56.055-20.496x-334.96x^2+1029.9x^3-1348.7x^4+835.73x^5-199.86x^6$$

Here, $x=\sin\theta/\lambda$.

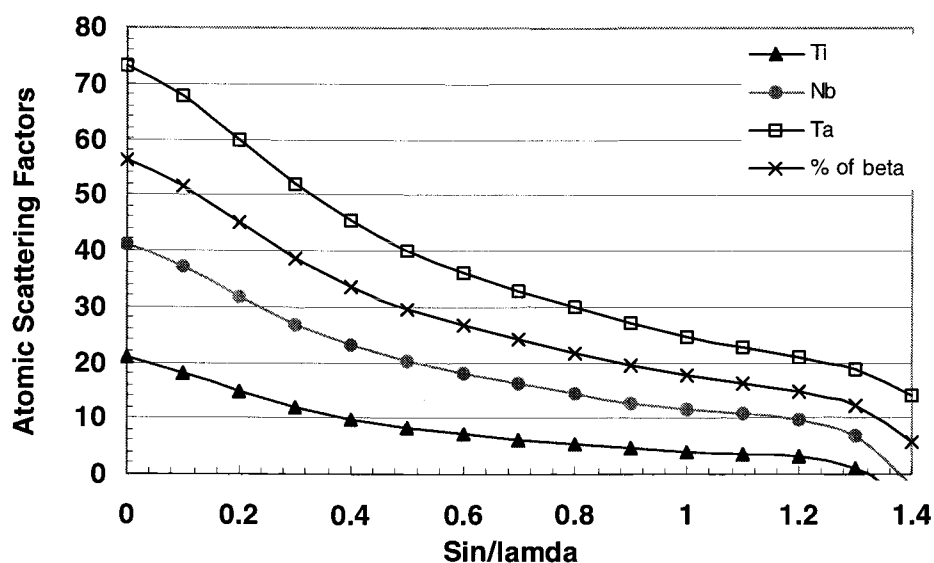


Figure A1. The atomic scattering factors. “% of beta” is taken from wt % of niobium and wt % tantalum. Nb24Ta49Ti is shown here. However, the difference between the average value and percentage value is small. In this writing, average value is used for all ternary samples.

Appendix II. Regular Solution Models of Ternary Phase Equilibria

Ternary Phase:

This appendix contains derivation of regular solution models based on the model of Kaufman's ^[11]. This model has been applied explicitly in terms of the pairwise interaction parameters determined numerically. MATHEMATICA has been used to solve the equation systems for equilibrium between the solution phases (α and β). The governing equation is shown as:

$$F^\alpha[x^\alpha, x^\beta \dots x^n, T] = \sum_{i=1}^n x_i F_i^\alpha[T] - T \Delta S + \sum_{i=1}^n \sum_{j=1}^n x_i x_j E_{ij}^\alpha \quad \text{Equation A6}$$

$$\sum_{i=1}^n x_i = 1$$

$$\Delta S = -R \sum_{i=1}^n x_i \ln x_i \quad \text{Equation A6.1}$$

Notations are listed in Table A2.

Where: x_i is the atomic fraction of element i , T is the absolute temperature in Kelvin, F_i^α $[T]$ is the free energy of pure element i in α phase, and E_{ij}^α is the α structure interaction parameter between elements i and j . This equation is the extension of the regular solution model which has been applied to binary systems in equation 4.

The equilibration of the partial free energies of i , j , and k across the two-phase region, as shown in Figure A2 is:

$$\begin{aligned} \bar{F}_i^\alpha(x_\alpha, y_\alpha) &= \bar{F}_i^\beta(x_\beta, y_\beta) \\ \bar{F}_j^\alpha(x_\alpha, y_\alpha) &= \bar{F}_j^\beta(x_\beta, y_\beta) \\ \bar{F}_k^\alpha(x_\alpha, y_\alpha) &= \bar{F}_k^\beta(x_\beta, y_\beta) \end{aligned} \quad \text{Equation A7}$$

Where the partial molar free energies of i, j, k in the α and β phases are given by:

$$\begin{aligned}
 \overline{F}_i^\alpha &= F^\alpha - x \frac{\partial F^\alpha}{\partial x} - y \frac{\partial F^\alpha}{\partial y} \\
 &= F_i^\alpha + RT \ln z + x^2 E_{ij}^\alpha + y^2 E_{ik}^\alpha + xy \Delta E^\alpha \\
 \overline{F}_j^\alpha &= F^\alpha - (1-x) \frac{\partial F^\alpha}{\partial x} - y \frac{\partial F^\alpha}{\partial y} \\
 &= F_j^\alpha + RT \ln x + (1-x)^2 E_{ij}^\alpha + y^2 E_{ik}^\alpha + (1-x)y \Delta E^\alpha \\
 \overline{F}_k^\alpha &= F^\alpha - x \frac{\partial F^\alpha}{\partial x} + (1-y) \frac{\partial F^\alpha}{\partial y} \\
 &= F_k^\alpha + RT \ln y + x^2 E_{ij}^\alpha + (1-y)^2 E_{ik}^\alpha - x(1-y) \Delta E^\alpha \\
 \Delta E^\alpha &= E_{ij}^\alpha + E_{ik}^\alpha - E_{jk}^\alpha
 \end{aligned}
 \tag{Equation A8}$$

The other partial free energies are defined similarly. Combining equation A6, A7 and A8 yields three equations relating x_α , y_α , x_β , y_β , and T:

$$\begin{aligned}
 F_i^\alpha - F_i^\beta &= \Delta F_i^{\beta \rightarrow \alpha} + RT \ln \left(\frac{z_\beta}{z_\alpha} \right) + (E_{ij}^\alpha x_\beta^2 - E_{ij}^\beta x_\alpha^2) + (E_{ik}^\alpha y_\beta^2 - E_{ik}^\beta y_\alpha^2) + (\Delta E^\beta x_\beta y_\beta - \Delta E^\alpha x_\alpha y_\alpha) = 0 \\
 F_j^\alpha - F_j^\beta &= \Delta F_j^{\beta \rightarrow \alpha} + RT \ln \left(\frac{x_\beta}{x_\alpha} \right) + (E_{ij}^\alpha (1-x_\beta)^2 - E_{ij}^\beta (1-x_\alpha)^2) + (E_{ik}^\alpha y_\beta^2 - E_{ik}^\beta y_\alpha^2) \\
 &\quad - (\Delta E^\beta (1-x_\beta) y_\beta - \Delta E^\alpha (1-x_\alpha) y_\alpha) = 0 \\
 F_k^\alpha - F_k^\beta &= \Delta F_k^{\beta \rightarrow \alpha} + RT \ln \left(\frac{y_\beta}{y_\alpha} \right) + (E_{ij}^\alpha x_\beta^2 - E_{ij}^\beta x_\alpha^2) + (E_{ik}^\alpha (1-y_\beta)^2 - E_{ik}^\beta (1-y_\alpha)^2) \\
 &\quad - (\Delta E^\beta (1-y_\beta) x_\beta - \Delta E^\alpha (1-y_\alpha) x_\alpha) = 0
 \end{aligned}$$

Equation A9

Table A2. The notations used in NbTiTa ternary system

	Niobium	Titanium	Tantalum
At. % of elements	Z	Y	X
Elements	I	K	J

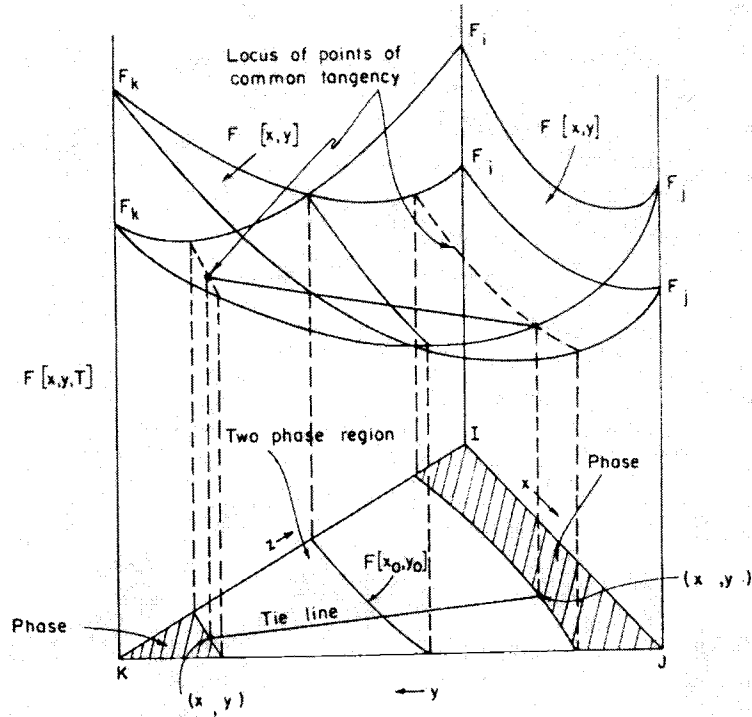


Figure A2. Free energy representation of the formation of ternary-solution phase equilibria. The phase diagram projected below results from the interaction of free energy surface as shown^[11].

Binary Phase:

For binary system, the equation A6 reduced to:

$$F^\alpha[x^\alpha, x^\beta, T] = (1-x)F_i^\alpha + xF_j^\alpha + RT[x \ln x + (1-x) \ln(1-x)] + E_{xs}^\alpha \text{ cal/g-atom}$$

Equation A10

E_{xs}^α is the excess free energy of the mixing which is zero when $x=0$ and 1 . In regular solution model, the excess free energy is given by $E_{xs}^\alpha = B x (1-x)$ cal/g - atom where: B is the interaction parameter and $B=0$ for ideal solution.

The partial free energy of components i and j is:

$$\begin{aligned}\bar{F}_i^\alpha &= F_i^\alpha - x \frac{\partial F^\alpha}{\partial x} \\ \bar{F}_j^\alpha &= F_j^\alpha - (1-x) \frac{\partial F^\alpha}{\partial x}\end{aligned}\quad \text{Equation A11}$$

Notice that the equation A11 is reduced from equation A8.

Now, we take partial derivatives respect to the x according to equation A10:

$$\begin{aligned}\frac{\partial F^\alpha}{\partial x} &= -F_i^\alpha + (1-x) \frac{\partial F_i^\alpha}{\partial x} + F_j^\alpha + x \frac{\partial F_j^\alpha}{\partial x} + B(1-x) - Bx + RT[\ln x + 1 - \ln(1-x) - 1] \\ &= -F_i^\alpha + F_j^\alpha + B - 2Bx + RT[\ln x - \ln(1-x)]\end{aligned}\quad \text{Equation A12}$$

Insert equation A10 and A12 into A11, we have:

$$\begin{aligned}\bar{F}_i^\alpha &= (1-x)F_i^\alpha + xF_j^\alpha + RT[x \ln x + (1-x) \ln(1-x)] + Bx(1-x) \\ &\quad - x\{-F_i^\alpha + F_j^\alpha + B - 2Bx + RT[\ln x - \ln(1-x)]\} \\ &= F_i^\alpha + RT \ln(1-x) + Bx^2\end{aligned}\quad \text{Equation A14}$$

$$\text{Similarly, } \bar{F}_j^\alpha = F_j^\alpha + RT \ln x + B(1-x)^2 \quad \text{Equation A15}$$

x is at % of element of j . Similar expression can be obtained for β phase.

$$\bar{F}_i^\beta = F_i^\beta + RT \ln(1-x) + Bx^2 \quad \text{Equation A16}$$

$$\bar{F}_j^\beta = F_j^\beta + RT \ln x + B(1-x)^2 \quad \text{Equation A17}$$

Applying the equilibrium conditions:

$$\begin{aligned}\bar{F}_i^\alpha \Big|_{x_\alpha} &= \bar{F}_i^\beta \Big|_{x_\beta} \\ \bar{F}_j^\alpha \Big|_{x_\alpha} &= \bar{F}_j^\beta \Big|_{x_\beta}\end{aligned}\quad \text{Equation A18}$$

Combination of equation A14-A18 yields

$$F_i^\alpha - F_i^\beta = \Delta F_i^{\beta \rightarrow \alpha} = RT \ln \left(\frac{1-x^\alpha}{1-x^\beta} \right) + B(x^\beta)^2 - A(x^\alpha)^2 \quad \text{Equation A19}$$

$$F_j^\alpha - F_j^\beta = \Delta F_j^{\beta \rightarrow \alpha} = RT \ln \left(\frac{x^\alpha}{x^\beta} \right) + B(1 - x^\beta)^2 - A(1 - x^\alpha)^2 \quad \text{Equation A20}$$

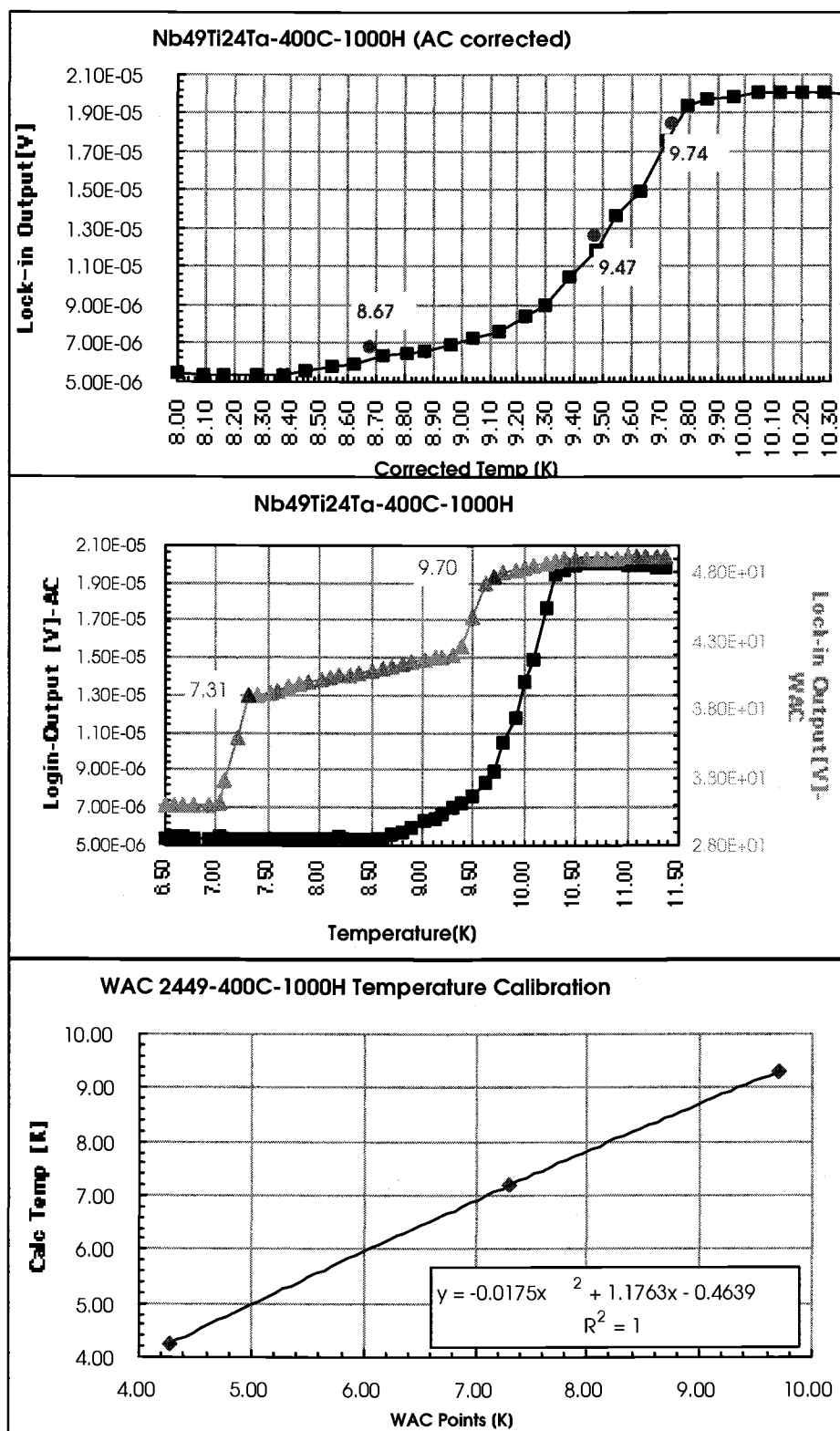
where: A and B are the regular solution interaction parameters for the hcp and bcc phase in i-j systems. Simultaneous solution of A19 and A20 yields the equilibrium composition of the α and β phases.

Appendix III Critical Temperature Measurement

The data acquisition software adjusts the temperature set points, waits for stable temperature, and then records the lock-in amplifier output. The data pair of lock-in output and temperature is recorded and a new temperature set point is determined. Thus, the change in magnetic susceptibility of the sample is recorded, as shown in Figure a.

The starting point of the Tc transition in each of two witness coils and the on-site liquid-helium-temperature are recorded as the critical temperatures of pure niobium, pure lead, and liquid helium. These three points with ideal critical temperatures of these three points ($T_{c(NB)} = 9.3$, $T_{c(PB)} = 7.2$, $T_{c(OK)} = 4.2$) are plotted, and fitted with quadratic function, as shown in Figure b. According to this quadratic fit function, the Tc data is replotted with calibration data points, as shown in Figure c. Then, a corrected critical temperature of the sample is determined from the 10%, 50% and 90% transition height data. 50% of Tc is reported as our critical temperature.

Figure A3. Critical Temperature Measurement



Appendix IV-Critical Temperature Data

Figure A4. The Critical Temperature Verses the Heat Treatment

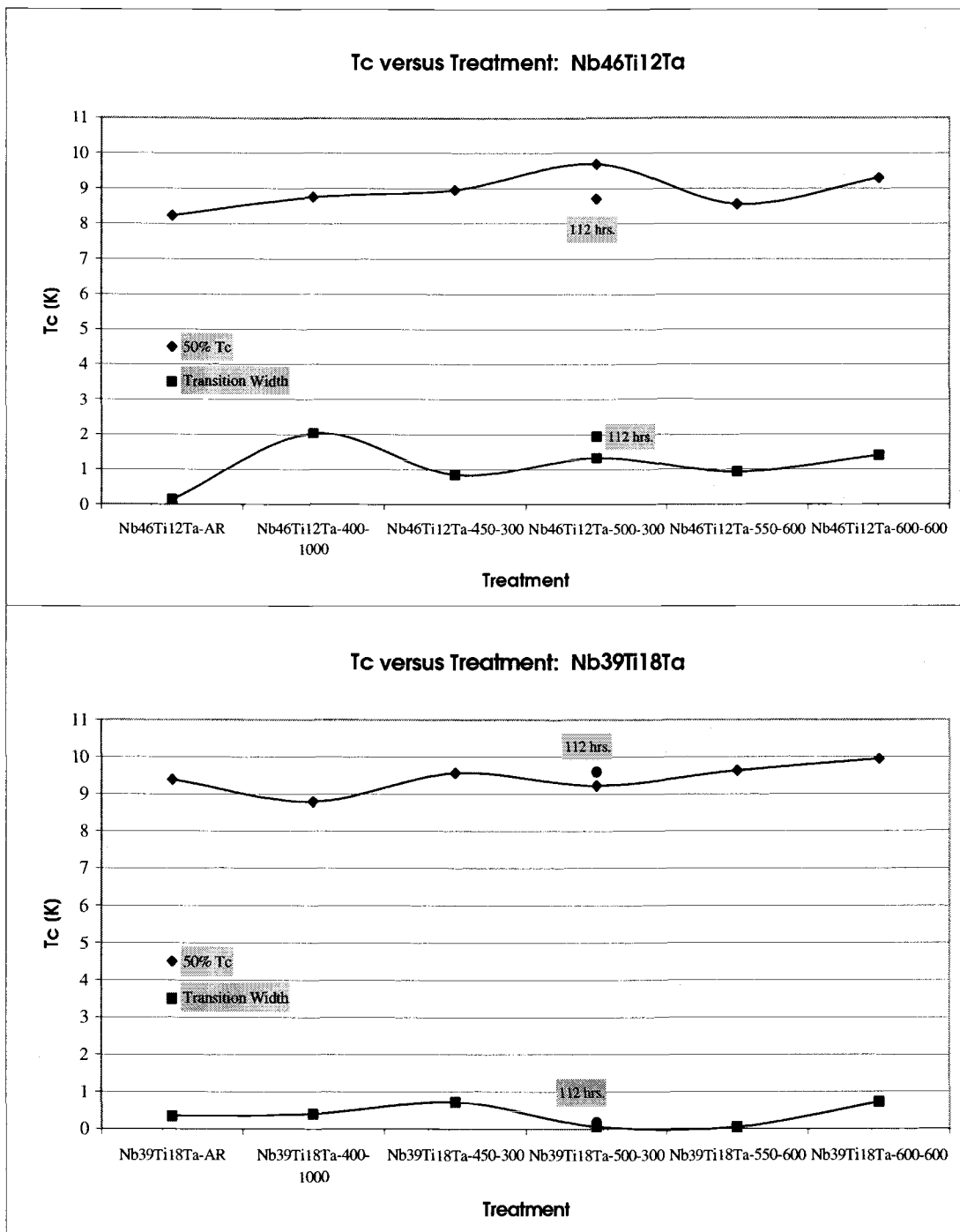


Figure A4. The Critical Temperature Verses the Heat Treatment-Continued

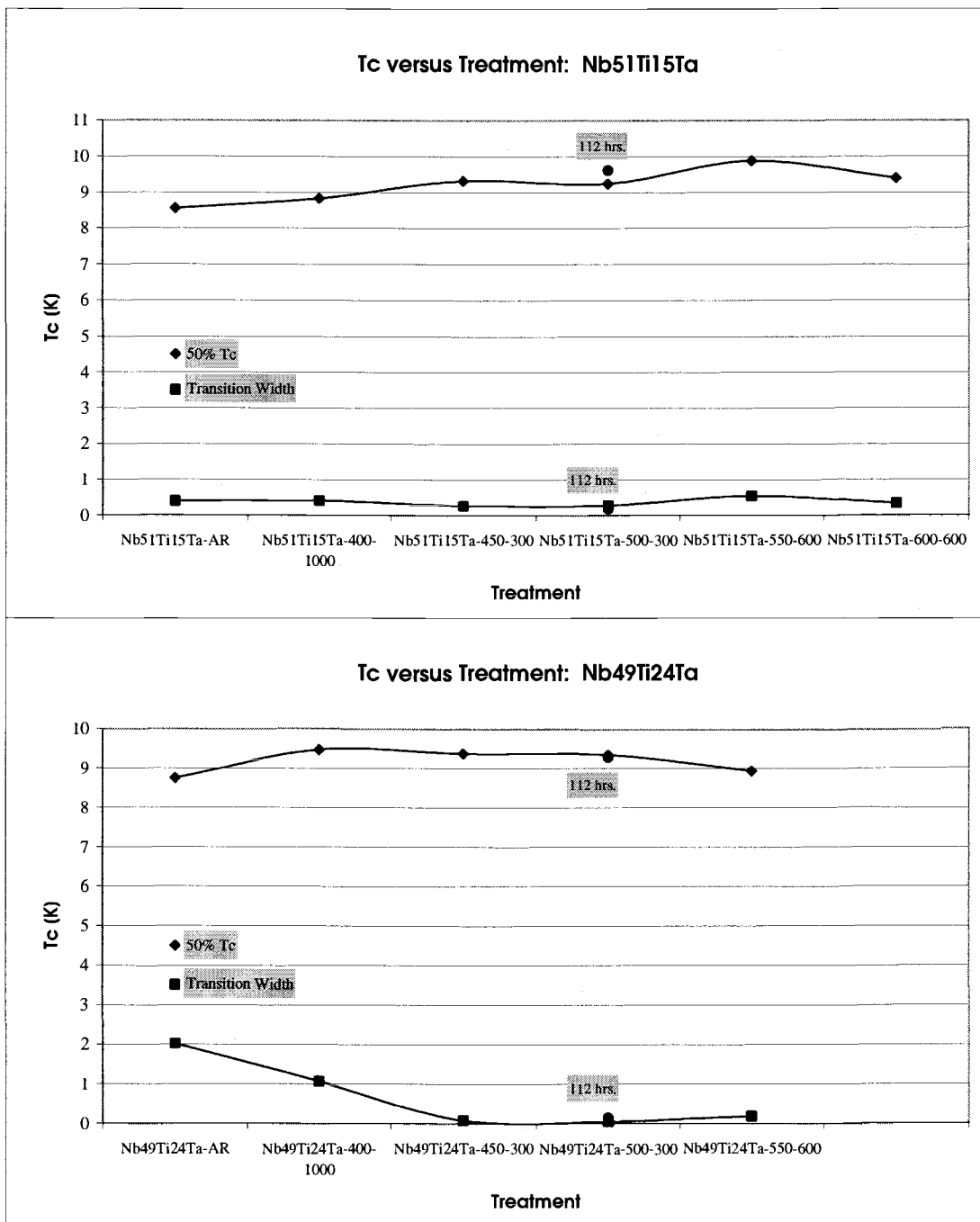


Figure A4. The Critical Temperature Verses the Heat Treatment-Continued

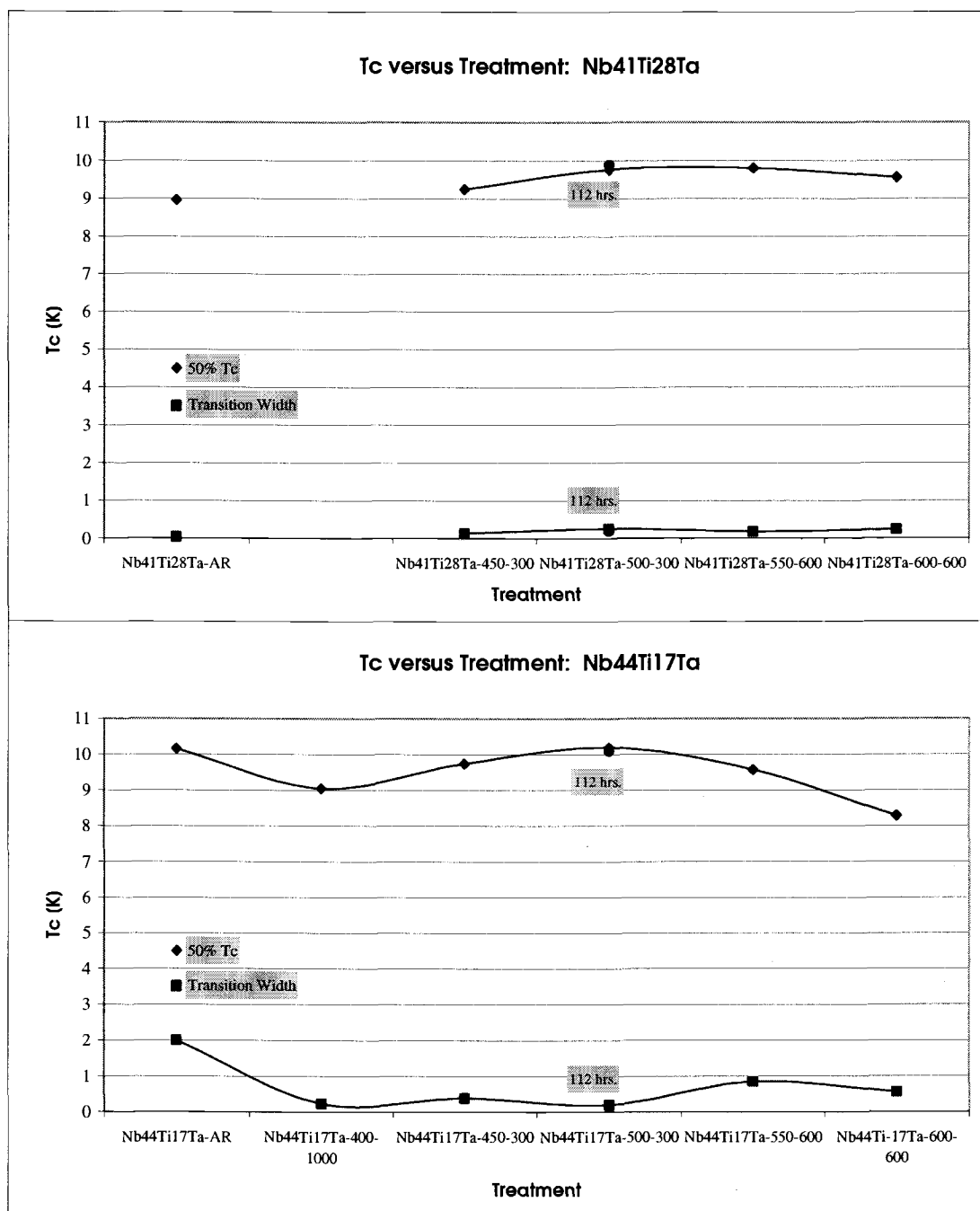


Figure A4. The Critical Temperature Verses the Heat Treatment-Continued

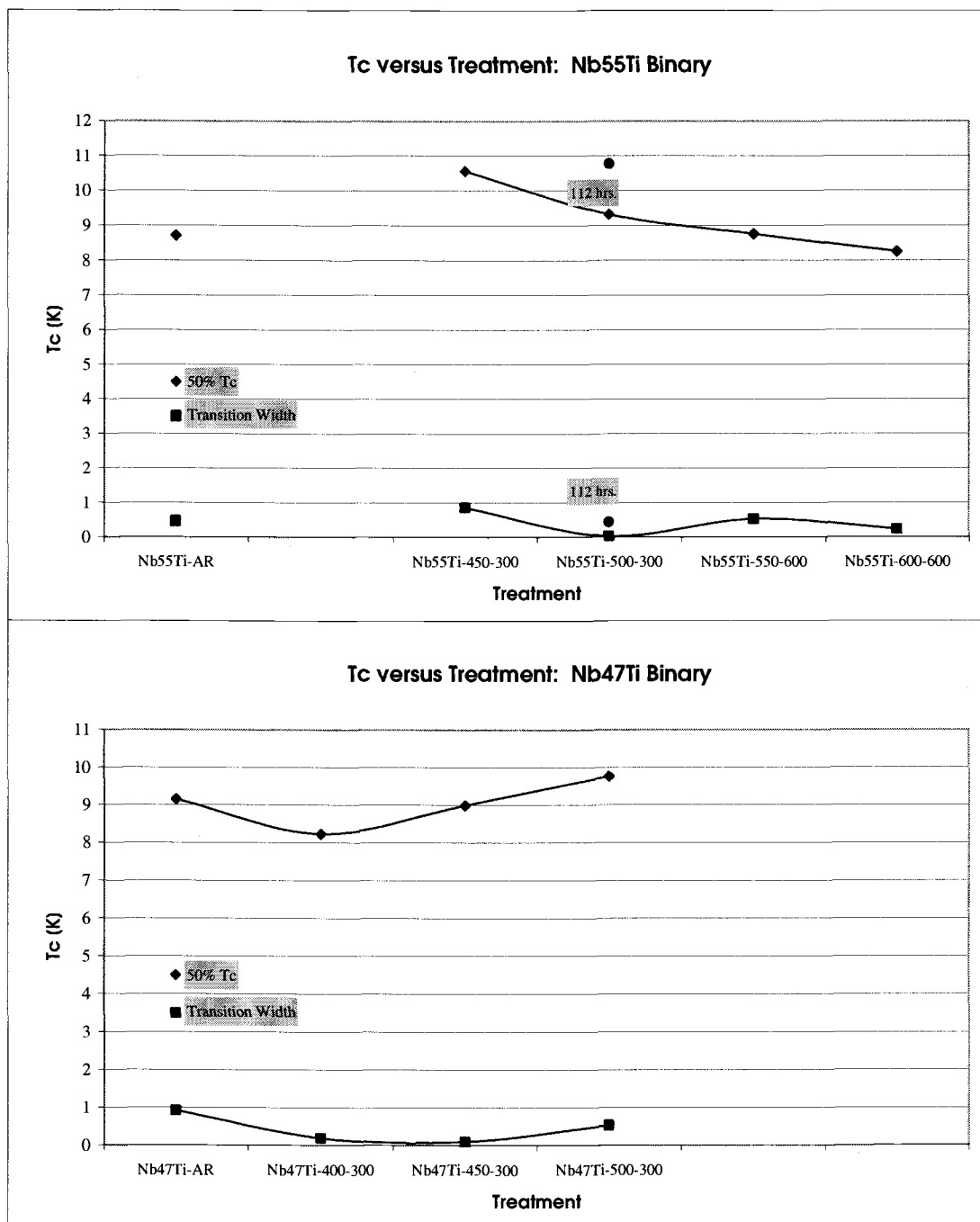


Figure A4. The Critical Temperature Verses the Heat Treatment-Continued

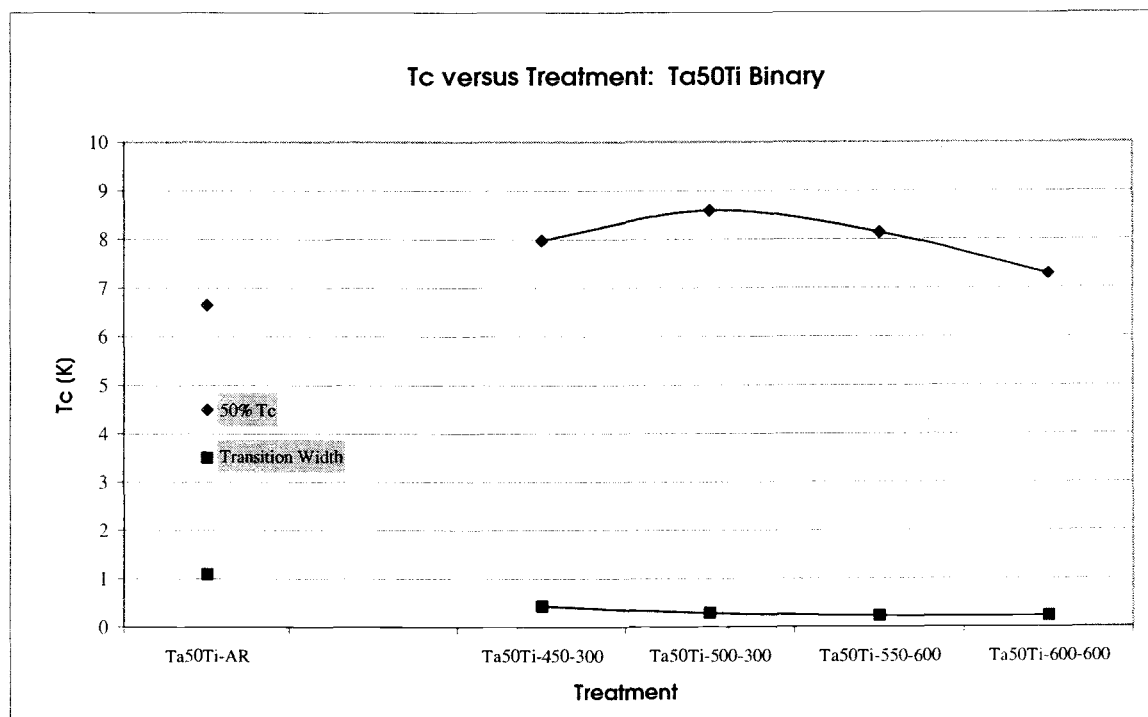


Table A3. Critical Temperatures at different aging temperatures and aging times.

Sample Name	10%Tc	50%Tc	90%Tc	Δ Tc
Nb46Ti12Ta-AR	8.15	8.23	8.29	0.14
Nb51Ti15Ta-AR	8.4	8.55	8.8	0.4
Nb44Ti17Ta-AR	8.7	10.15	10.7	2
Nb39Ti18Ta-AR	9.21	9.39	9.55	0.34
Nb49Ti24Ta-AR	7.5	8.75	9.52	2.02
Nb41Ti28Ta-AR	8.94	8.96	8.98	0.04
Nb47Ti-AR	8.53	9.15	9.45	0.92
Nb55Ti-AR	8.42	8.7	8.87	0.45
Ta50Ti-AR	6.13	6.65	7.22	1.09
Nb46Ti12Ta-400-1000	7.39	8.74	9.43	2.04
Nb51Ti15Ta-400-1000	8.65	8.83	9.06	0.41
Nb44Ti17Ta-400-1000	8.92	9.04	9.15	0.23
Nb39Ti18Ta-400-1000	8.6	8.8	9	0.4
Nb49Ti24Ta-400-1000	8.67	9.47	9.74	1.07
Nb41Ti28Ta-400	N/A	N/A	N/A	N/A
Nb47Ti-400-300	8.13	8.23	8.32	0.19
Ta50Ti-400	N/A	N/A	N/A	N/A
Nb46Ti12Ta-450-300	8.35	8.95	9.2	0.85
Nb51Ti15Ta-450-300	9.14	9.32	9.41	0.27
Nb44Ti17Ta-450-300	9.46	9.74	9.85	0.39
Nb39Ti18Ta-450-300	9.18	9.57	9.89	0.71
Nb49Ti24Ta-450-300	9.3	9.37	9.38	0.08
Nb41Ti28Ta-450-300	9.14	9.25	9.28	0.14
Nb47Ti-450-300	8.96	8.99	9.06	0.1
Nb55Ti-450-300	10.1	10.56	10.96	0.86
Ta50Ti-450-300	7.63	7.98	8.06	0.43
Nb46Ti12Ta-500-300	9.01	9.69	10.33	1.32
Nb51Ti15Ta-500-300	9.09	9.24	9.37	0.28
Nb44Ti17Ta-500-300	10.03	10.19	10.23	0.2
Nb39Ti18Ta-500-300	9.2	9.23	9.26	0.06
Nb49Ti24Ta-500-300	9.3	9.34	9.35	0.05
Nb41Ti28Ta-500-300	9.61	9.76	9.87	0.26
Nb47Ti-500-300	9.44	9.76	9.97	0.53
Nb55Ti-500-300H	9.29	9.31	9.32	0.03
Ta50Ti-500-300	8.41	8.59	8.7	0.29
Nb46Ti12Ta-550-600	8.07	8.55	9	0.93
"-550-300"	7.22	7.68	8.35	1.13
Nb51Ti15Ta-550-600	9.67	9.88	10.21	0.54
Nb44Ti17Ta-550-600	9.1	9.56	9.95	0.85
Nb39Ti18Ta-550-600	9.61	9.63	9.65	0.04
Nb49Ti24Ta-550-600	8.8	8.93	8.99	0.19
Nb41Ti28Ta-550-600	9.7	9.8	9.88	0.18
Nb55Ti-550-600	8.3	8.75	8.83	0.53
Ta50Ti-550-600	7.99	8.14	8.22	0.23
Nb46Ti12Ta-600-600	8.65	9.29	10.05	1.4

Table A3. Critical Temperatures at Different Aging Temperatures and Aging Times-Continued.

Nb51Ti15Ta-600-600	9.21	9.39	9.55	0.34
Nb49Ti24Ta-600-600	6.83	7.08	7.31	0.48
Nb44Ti-17Ta-600-600	7.91	8.28	8.47	0.56
Nb39Ti18Ta-600-600	9.46	9.95	10.18	0.72
Nb41Ti28Ta-600-600	9.44	9.56	9.68	0.24
Nb55Ti-600-600	8.13	8.25	8.36	0.23
Ta50Ti-600-600	7.17	7.29	7.4	0.23
Nb46Ti12Ta-500-112	7.12	8.7	9.06	1.94
Nb51Ti15Ta-500-112	9.53	9.61	9.71	0.18
Nb44Ti17Ta-500-112	10.02	10.09	10.14	0.12
Nb39Ti18Ta-500-112	9.54	9.6	9.71	0.17
Nb49Ti24Ta-500-112	9.21	9.28	9.36	0.15
Nb41Ti28Ta-500-112	9.74	9.88	9.94	0.2
Nb47Ti-500-112	N/A	N/A	N/A	N/A
Nb55Ti-500-112	10.64	10.77	11.08	0.44
Pure NB sheet	8.91	9.00	9.08	0.17